

AD _____

GRANT NUMBER DAMD17-94-J-4424

TITLE: Single-Pulse Dual-Energy Mammography Using a Binary
Screen Coupled to Dual CCD Cameras

PRINCIPAL INVESTIGATOR: John M. Boone, Ph.D.

CONTRACTING ORGANIZATION: University of California
Davis, California 95616-8671

REPORT DATE: August 1997

TYPE OF REPORT: Annual

PREPARED FOR: Commander
U.S. Army Medical Research and Materiel Command
Fort Detrick, Frederick, Maryland 21702-5012

DISTRIBUTION STATEMENT: Approved for public release;
distribution unlimited

The views, opinions and/or findings contained in this report are those of the author(s) and should not be construed as an official Department of the Army position, policy or decision unless so designated by other documentation.

19980220 083

DTIC QUALITY INSPECTED 4

REPORT DOCUMENTATION PAGE

Form Approved
OMB No. 0704-0188

Public reporting burden for this collection of information is estimated to average 1 hour per response, including the time for reviewing instructions, searching existing data sources, gathering and maintaining the data needed, and completing and reviewing the collection of information. Send comments regarding this burden estimate or any other aspect of this collection of information, including suggestions for reducing this burden, to Washington Headquarters Services, Directorate for Information Operations and Reports, 1215 Jefferson Davis Highway, Suite 1204, Arlington, VA 22202-4302, and to the Office of Management and Budget, Paperwork Reduction Project (0704-0188), Washington, DC 20503.

1. AGENCY USE ONLY (Leave blank)		2. REPORT DATE August 1997	3. REPORT TYPE AND DATES COVERED Annual (15 Jul 96 - 14 Jul 97)	
4. TITLE AND SUBTITLE Single-Pulse Dual-Energy Mammography Using a Binary Screen Coupled to Dual CCD Cameras			5. FUNDING NUMBERS DAMD17-94-J-4424	
6. AUTHOR(S) John M. Boone, Ph.D.				
7. PERFORMING ORGANIZATION NAME(S) AND ADDRESS(ES) University of California Davis, California 95616-8671			8. PERFORMING ORGANIZATION REPORT NUMBER	
9. SPONSORING/MONITORING AGENCY NAME(S) AND ADDRESS(ES) Commander U.S. Army Medical Research and Materiel Command Fort Detrick, Frederick, Maryland 21702-5012			10. SPONSORING/MONITORING AGENCY REPORT NUMBER	
11. SUPPLEMENTARY NOTES				
12a. DISTRIBUTION / AVAILABILITY STATEMENT Approved for public release; distribution unlimited			12b. DISTRIBUTION CODE	
13. ABSTRACT (Maximum 200) Progress on several fronts has been made towards the completion of the Statement of Work on this grant. X-ray spectra from a mammographic system and from a general diagnostic x-ray system were characterized using a technique developed by the principal investigator. These spectral models are useful in performing computer simulations for the purpose of optimizing the design of the dual energy mammography system which is the focus of this research. We have evaluated scintillator systems as an alternative to screen film systems. Monte Carlo calculations of the normalized glandular dose for different breast thicknesses and x-ray spectra have been performed, and we are in the process of evaluating results and refining the Monte Carlo model. We have begun a series of experiments in which we hope to verify many aspects of the computer simulated calculations. Dual energy images have been acquired, although we have yet to develop an anatomically similar phantom of the breast. The physical design of the dual energy imaging system has been modified in response to our ongoing research results, and towards the end of this fiscal year we hope to have a fully operational, optimized prototype (small field of view) digital mammography system in our laboratory.				
14. SUBJECT TERMS Breast Cancer Monte Carlo Dual Energy Digital Mammography			15. NUMBER OF PAGES 49	
			16. PRICE CODE	
17. SECURITY CLASSIFICATION OF REPORT Unclassified	18. SECURITY CLASSIFICATION OF THIS PAGE Unclassified	19. SECURITY CLASSIFICATION OF ABSTRACT Unclassified	20. LIMITATION OF ABSTRACT Unlimited	

FOREWORD

Opinions, interpretations, conclusions and recommendations are those of the author and are not necessarily endorsed by the U.S. Army.

____ Where copyrighted material is quoted, permission has been obtained to use such material.

____ Where material from documents designated for limited distribution is quoted, permission has been obtained to use the material.

JMB Citations of commercial organizations and trade names in this report do not constitute an official Department of Army endorsement or approval of the products or services of these organizations.

____ In conducting research using animals, the investigator(s) adhered to the "Guide for the Care and Use of Laboratory Animals," prepared by the Committee on Care and Use of Laboratory Animals of the Institute of Laboratory Resources, National Research Council (NIH Publication No. 86-23, Revised 1985).

JMB For the protection of human subjects, the investigator(s) adhered to policies of applicable Federal Law 45 CFR 46.

____ In conducting research utilizing recombinant DNA technology, the investigator(s) adhered to current guidelines promulgated by the National Institutes of Health.

____ In the conduct of research utilizing recombinant DNA, the investigator(s) adhered to the NIH Guidelines for Research Involving Recombinant DNA Molecules.

____ In the conduct of research involving hazardous organisms, the investigator(s) adhered to the CDC-NIH Guide for Biosafety in Microbiological and Biomedical Laboratories.


PI Signature

29 SEPT 97
Date

4. Table of Contents

Single-Pulse Dual-Energy Mammography using a binary screen coupled to dual CCD cameras

1. Cover Page	i
2. Report Documentation Page	ii
3. Foreword	iii
4. Table of Contents	1
5. Introduction	2
5.1 Background	2
Breast Cancer and Mammography	2
Administrative Issues	2
Statement of Work	4
6. Body of Report	6
6.1 Computer based spectral models	6
6.2 Physical measurement of spectra	7
6.3 Alternate scintillator systems	8
6.4 Monte Carlo modeling	10
6.5 Monte Carlo Analysis of Dg_N	11
6.6 Scatter suppression	13
6.7 Dual energy imaging	14
6.8 Figures 1-37	16-37
7. Conclusions	38
8. References	39
9. Appendix A - List of Grant Sponsored Publications	41
Appendix B - Derivation of Spectrometer Correction Factors	42

5. Introduction

5.1 Background

Breast Cancer and Dual Energy Mammography

Breast cancer will strike approximately one in nine women in the United States, making it the most common form of cancer amongst women. In 1992, there were over 46,000 deaths due to breast cancer and 180,000 new cases were detected. Presently, there is no cure for this devastating disease and the best hope for patients stricken with breast cancer lay in its early detection. While ultrasound and MRI are modalities that have been aimed at the breast, x-ray mammography has the best sensitivity for the early detection of breast cancer in women who are asymptomatic. Hence, mammography has proliferated substantially over the last 10 years as an important "front line" against breast cancer.

Digital mammography systems have been under development for over a decade, and presently several commercial systems by General Electric, Fischer, and Trex Medical are being tested in clinical trials. No doubt the reader is familiar with the various technologies currently being developed for digital mammography, and an extensive description will therefore be avoided for brevity. While the dynamic range and probably the DQE(f) of digital mammography systems will be superior to film, it is likely that the dense breast is an area that will still pose a challenge for diagnostic evaluation, because the anatomic noise in the image can overwhelm the observer and obscure the visibility of a breast cancer lesion. The central purpose of this US Army Breast Cancer Research Program grant is to develop a dual energy mammography system, and evaluate its potential for increasing the visibility of microcalcifications in the dense breast by reducing anatomical noise.

The analysis of the effectiveness of dual energy mammography was to be performed initially using a binary screen detector system, alluded to in the title of the grant. The binary screen system¹ is basically a two component phosphor screen, where one component is a green emitting $\text{Gd}_2\text{O}_2\text{S}$ and the other is a red emitting $\text{Y}_2\text{O}_2\text{S}$. Because the k-edge of Y is approximately 19 keV and that of Gd is 50 keV, the higher energy x-rays will be preferentially absorbed by the $\text{Gd}_2\text{O}_2\text{S}$ and the lower energy x-rays by the $\text{Y}_2\text{O}_2\text{S}$. By focusing two CCD cameras onto the binary screen, one camera green-filtered, the other red-filtered, the acquisition of an x-ray exposure to the detectors allows the high energy component of the beam to be preferentially detected by the green channel CCD and the low energy component of the beam is preferentially detected by the red channel CCD. While the binary screen system allows good energy separation in a single pulse of x-rays, it is not as good as the energy separation achievable by using a combination of kV-switching and pre-patient filtration. Therefore, in the first year of the proposal we changed our search for the optimal binary screen, single pulse system to the optimal dual energy system using a combination of kV switching and filtration. We realized that what needs to be demonstrated is the very best that dual energy can do in terms of signal to noise ratio. The peer review analysis of our first year report concurred with this redirection.

5.1 Administrative Issues concerning this Grant

The US Army grant administration, responding to the study section comments at the time of funding this proposal back in late 1994, cut the budget by 27%, with the justification given that the study section recommended that the small scale clinical trial proposed near the end of the grant period be eliminated. After administrative contact with the US Army grant administration officials recently, the PI officially requested that the clinical trial component (all of Task 5) of the Statement of Work be eliminated, since the funding for it was cut. This request (which was put forward at the suggestion of

the US Army administrators) was approved. Therefore, we have been preceding at a pace necessary to complete tasks 1 through 4, but not necessarily in that order.

5.2 Statement of Work

The original statement of work follows.

Task 1: Computer Simulation of Dual-Energy Digital Mammography System [months 1-24]

- 1.1. The most efficient x-ray spectrum, which depends on the anode target material (Molybdenum or Tungsten), the kilovoltage, and the thickness and composition of the pre-patient filter, will be identified for dual energy mammography
- 1.2. The most efficient x-ray spectrum, which depends on the anode target material (Molybdenum or Tungsten), the kilovoltage, and the thickness and composition of the pre-patient filter, will be identified for single energy mammography
- 1.3. The best thickness and phosphor ratio (e.g. mg Y_2O_3S versus mg Gd_2O_3S) for dual energy mammography will be identified using computer simulation with a typical breast thickness (4.2 cm).
- 1.4. The most efficient anti-scatter grid ratio and construction will be identified using the figure of merit $[SNR]^2 / [Average\ Glandular\ Dose]$

Task 2: Design and Construct Dual-Energy Mammography Imaging System [months 1-24]

- 2.1. Consult with mechanical engineer (consultant on project) and finalize design for the mechanical construction of the system housing, and have EOT, Inc build it.
- 2.2. Purchase optical supports and cameras, and mount them inside the completed housing (2.A). Interface optical and electronic components to microcomputer, and microcomputer to x-ray generator. Write software to orchestrate both auto-calibration procedures as well as digital image acquisition.

Task 3: Measure performance of digital mammography system [months 24-36]

- 3.1. Measure the MTF of the system, and optimize alignment, focus and acquisition to assure maximum spatial resolution
- 3.2. Measure the DQE of the system. Also estimate the figure of merit, $[SNR]^2/Dose$, for a range of acquisition parameters (e.g. grid or no-grid, kV, object thickness).
- 3.3. Digitize film images taken under identical technique settings (kV & mAS), and compare contrast to noise ratio and spatial resolution

Task 4: Evaluate algorithms for the processing and display of the dual-energy and single energy images. [months 24-40]

- 4.1. Investigate potential of neural network to perform both noise suppression and dual-energy subtraction in a single pass.
- 4.2. Write software to allow easy, mouse-driven interaction with the image data base and with the images as they are displayed. Develop algorithms to identify calcifications on the dual energy image, colorize them, and superimpose them onto the low-energy and/or the (low + high) energy images.

The following is included for historical reasons, but these tasks were eliminated by the peer review study section and by a commensurate cut in funding by the US Army.

Task 5: Perform a limited clinical study comparing the performance of the digital system with film-screen mammography. [months 36-48]

- 5.1. Recruit patients who have mammographically-identified lesions, and after receiving consent, make images of the area(s) of the breast which contain the lesions.
 - 5.2. Make visual comparisons between the screen-film images and those acquired with the digital system. Digitize the film-screen images on a laser scanner and compare both image types in digital format. Make measurements of contrast to noise ratio on both digitized film images and on the acquired digital mammograms. Compare.
-

6. Body of Report

6.1 Computer Based Spectral Models

For computer simulation purposes, it is convenient to be able to produce realistic x-ray spectra using a computer program. There have been many attempts at producing spectral computer models, including several by the PI²⁻⁴. In recent years, the computer modeling of Tucker^{5,6} has been probably the most used model in the radiology physics literature. Nevertheless, the seminal work of Tom Fewell^{7,8} and his colleagues at the Center for Devices and Radiological Health (CDRH) of physically measuring x-ray spectra remains the gold standard for accurate x-ray spectra.

For this dual energy mammography project, we require a very low energy beam (with an effective energy at about 19 keV^{9,10}) and a higher energy beam with an effective energy at about 70 keV^{9,10}. We sought to produce an accurate model of x-ray spectra, both for mammography x-ray systems which may use molybdenum, rhodium, or tungsten anodes, and for general diagnostic x-ray systems employing tungsten anodes, generally for kVs over 30 kV.

A spectral model based on the measured spectra of Fewell was developed for both general radiographic systems and dedicated mammography x-ray sources. The general diagnostic system will be described first. An x-ray system in our laboratory (a Toshiba 2000 mA constant potential generator with an 800,000 heat unit tungsten anode x-ray tube) was fully characterized in terms of its output, including the absolute output of the system (mR/mAS @ 100 cm, Figure 1) and the spectral quality as measured by aluminum attenuation profiles (Figure 2). Toshiba service personnel were present during the measurements, and they had just verified the accuracy of the kV settings on this system using voltage dividers. A recently cross-calibrated ionization meter (MDH 2025) was used for the exposure measurements. The output and filtered output data (Figures 1 and 2) were computer fit to analytical functions (TableCurve 2D, Jandel Scientific, Corta Madera, CA).

The published measured x-ray spectra of Fewell for tungsten anode CPG spectra were used to produce similar x-ray output and attenuation curves. Employing least square optimization procedures, a small amount of aluminum filtration was added mathematically to the tabulated Fewell spectra such that they were able to match the measured output and attenuation data generated in experimentally our laboratory. After these procedures, the modified Fewell spectra almost perfectly matched the output measurements of the x-ray system in our laboratory.

The tabulated x-ray spectra which described our x-ray system output were then characterized using a polynomial fitting procedure. A set of 11 x-ray spectra are shown in Figure 3. Each spectrum is normalized such that it corresponds to the output of the x-ray system in our laboratory at a setting of one mAS. There is a series of vertical lines shown in Figure 3, which intersect the x-ray spectra. These vertical lines (each at a different monoenergetic energy, keV) intersect the individual fluence values (photons/mm²/meter/mAs) of the spectra, each produced at a different x-ray tube voltage (kVp). The data corresponding to the intersections of the vertical lines with the spectral values (Figure 3) are illustrated in Figures 4 and 5. Notice that when the spectral data are plotted as shown in Figures 4 and 5, a smooth curve results. The points (symbols) on these graphs (Figures 4 and 5) correspond to the actual intersection points, while the curves (solid line) were generated by fitting the data points to a polynomial function. Notice that, because the curves are so smooth, the polynomial functions (which range in order from 2 to 5 terms) do an excellent job at interpolating the data. Thus, the term *interpolating polynomials* was used to describe this spectral model. Figures 4 and 5 illustrate curves for a total of 6 energies, but

an entire series of polynomial fit curves were produced. One set of polynomial coefficients describing each energy bin (at 1.0 keV intervals for this data) in the spectra was produced, ranging from 10 keV to 140 keV. These curves describe the x-ray fluence at a given energy (keV) as a function of a given tube potential (kVp). Using these polynomial fit data at each energy (keV), a spectrum at an arbitrary x-ray tube voltage (kVp) can be produced simply by computing the polynomial equations with the desired kVp. Examples of computer generated spectra are shown along with the parent spectra in Figures 6A-D. The spectral model described above has been dubbed the Tungsten Anode Spectral Model using Interpolating Polynomials ("TASMIP"). Using TASMIP, x-ray spectra were generated for a single mAs over a series of kVs, and compared to the original output data, physically measured in our laboratory (Figure 7). An excellent correspondence between the output of the model and measured spectra was observed. With a good model of x-ray spectra, we then generated a series of x-ray spectra with different amounts of filtration and kVs and computed the number of photons/mm²/mR. Despite the several parameters used in generating the x-ray spectra including kV, added Al filtration, kV waveform ripple, the data was well characterized by the HVL (Figure 8). A manuscript describing the TASMIP model (listed at reference 7 in Appendix A) has been accepted for publication in *Medical Physics*.

The same interpolating polynomial procedure was applied to a series of mammography x-ray system data recently measured by Fewell (not published; the PI was given the data on a floppy disk at the CDRH in November of 1995). X-ray spectra were characterized for tube voltages ranging from 18 to 42 kVp, and for molybdenum, rhodium, and tungsten anodes. The measured x-ray spectra were measured without any added filtration, whereas filtration is normally used in clinical mammography. This was done because the spectra could be better characterized unmasked by the influence of added filtration. It was also recognized that any added filtration could be added mathematically using a computer and a set of attenuation coefficients. Using the same procedure as that described above (except for the mammography spectra, the energy spacing was 0.5 keV), a series of computer-generated x-ray spectra are compared against Fewell's measured data. Figure 9 shows comparisons between three spectra taken at 20 kV, 30 kV, and 40 kV, for a molybdenum anode. The dotted lines correspond to the spectral model, the solid lines to the measured data. In most cases the fit is so good that the dotted line is obscured by the measured data line. Figure 10 illustrates the spectra for the rhodium anode, and Figure 11 shows the spectra for the tungsten anode. The molybdenum and rhodium spectra models were dubbed MASMIP and RASMIP, as the tungsten model was called TASMIP. A manuscript has been accepted for publication in *Medical Physics* describing this procedure for mammography x-ray system spectra.

The spectral models described above were produced so that our x-ray imaging computer simulations (e.g. dose analysis) and dual energy optimization procedures would be both more accurate, and would correspond better to results measured in the laboratory.

6.2 Physical Measurement of Spectra

Deslattes^{11,12} has developed an x-ray diffraction system designed originally to better determine the kV of mammography systems. The PI was fortunate to work with Dr. Deslattes (who is at NIST), and as a result we have a Deslattes diffractometer in our laboratory. The Deslattes diffraction device was developed under (separate) funding from the US Army BCRP. Whereas Deslattes originally designed the system for determining kV accurately, we were interested in having a device which is capable of measuring x-ray spectra. At our suggestion, Dr. Deslattes and his colleagues kindly and expertly redesigned the system to have lower theoretical energy resolution (this involved using a

different diffraction plane in the silicon crystal diffraction system, which also required a different bending and orientation of the crystal with respect to the x-ray beam). Using the modified diffraction system, we set out to develop corrections to the raw measured data so that the diffraction system could truly be called a spectrometer. To produce relatively accurate spectra from the Deslattes diffractometer, correction techniques need to be employed first to calibrate the energy axis, and also to calibrate the fluence axis of the spectrum. The procedures used for these calibrations are derived in Appendix B. Spectra were measured in our mammography facility on a GE 600T system, and were corrected using the techniques described in Appendix B. The corrected tungsten anode x-ray spectra were compared to the x-ray spectra measured by Fewell (using a germanium x-ray spectroscopy system), who used a similar x-ray system. The comparison x-ray spectra are illustrated in Figures 12A-D. This research has been written up, and will be submitted for publication in October.

6.3 Alternate Scintillator Systems

The purpose of this grant research is to demonstrate the maximal performance of dual-energy mammography. To do this, a dual-energy detector system was developed. While the system developed was never intended to be a clinically realistic system, it is our strong intention to produce a system which is capable of optimizing dual energy mammography detection performance. As mentioned in the introduction, the binary screen approach (Figure 13) has been abandoned because it will not yield the energy separation (or more importantly, the signal to noise ratio) of kV-switched or sandwiched dual energy detector system. We therefore went to a hybrid switched kV - sandwiched system (diagram in Figure 14, photograph in Figure 15). The hybrid system was thought to be able to provide the maximum SNR for a given dose for a dual energy system (more on this later).

The reader is probably aware of the need to develop a detector system which has no secondary quantum stages after x-ray detection. Using optically (lens based) coupled CCD cameras, however, leads to a situation where one is just on the edge of a secondary quantum sink^{13,14}. Nevertheless, given the 1994 inception of this proposal, a CCD based system was deemed the only way to produce a detector system using primarily off-the-shelf components. We have spent considerable analytical efforts towards fully understanding the constraints of optical coupling, and how to analyze such systems, and how to maximize their performance (resulting in articles 3, 4 and 6, listed in Appendix A). In the setup shown in Figure 14, we have estimated that we are measuring 4 electrons in the CCD camera per x-ray photon absorbed in the Min-R screen (front camera, low energy channel).

A Min-R screen ($34 \text{ mg/cm}^2 \text{ Gd}_2\text{O}_2\text{S:Tb}$) as the detector will have better spatial resolution than a Lanex intensifying screen ($60 \text{ mg/cm}^2 \text{ Gd}_2\text{O}_2\text{S:Tb}$), but it will have less light output. MTFs were measured for the aft screen/detector configuration (Figures 14 & 15) for both Min-R and Lanex screens, and these are shown in Figure 16. As expected, the Min-R screen outperforms Lanex at the higher spatial frequencies, but only slightly because of other factors which contribute towards a loss in spatial resolution. These factors include the focal spot (0.3 mm nominal) blurring due to high magnification (~ 1.25), and the optics and mirror MTFs. The MTFs are shown for the front screen/camera system in Figure 17.

Noise power spectra (NPS) were measured for both the Min-R and Lanex screens, and are shown for the transmission mode (aft) system (Figure 18) and for the reflection mode (front) system in Figure 19. In Figure 18 showing the transmission mode NPS, the Min-R screen has higher noise at zero spatial frequency as one would expect since it has reduced light emission. In the reflection mode, substantially higher light emission is achieved for both screens since most of the x-ray absorption in a screen is near

its front surface, especially at low energies. The NPS for the reflection mode are shown in Figure 19, and demonstrate less zero frequency noise than in the transmission mode. Also worth mentioning on the NPS plots is the fact that the NPS does not go to zero beyond the spatial frequencies where the MTF plots (Figures 16 & 17) do, indicating that substantial noise exists after the x-ray detection event. This is not surprising, given the existence of a possible quantum sink (especially at higher spatial frequencies) and some electronic noise.

The NPS were smoothed, and the DQE(f) were calculated and are shown in Figures 20 and 21. As expected, the DQE(f) for the lower energy reflection mode are better than the transmission mode. In addition, for the transmission mode, the front intensifying screen "steals" x-ray photons from the x-ray beam that do not result in signal in the back system. This front screen acts as a quantum sink for x-ray photons. While the front x-ray screen does act to filter out low energy x-ray photons from the high energy image, this leads to a reduction in the DQE of the aft detector as illustrated in Figure 20 (compared to 21). This consideration has lead us to consider a modification from the dual energy mammography system design, with the modified system illustrated in Figure 22.

The dual energy mammography system shown in Figure 22 demonstrates almost a complete turn of events from our initial binary single-x-ray pulse plans. Now that we found ourselves here it seems quite obvious. While a sandwich detector design allows single pulse imaging, it nevertheless represents a compromise in terms of image quality and dose, compared to a straightforward dual-pulse approach. With a dual pulse technique, the front part of the sandwiched detectors (Figure 14) is placed in front of the patient in the form of pre-patient filtration (Figure 22). In this manner, of course, the patient doesn't bear x-ray dose that is merely absorbed in the front screen. The reason why two cameras are necessary in the configuration shown in Figure 22 is that the read out time for these high resolution CCD systems is approximately 30 seconds, way too long between x-ray pulses. Using two cameras with a mirror that can be rapidly pivoted, two kV pulses can be achieved on our current x-ray system in approximately 30 msec (switching time).

Based upon further analysis of the detector performance in the configuration shown in Figure 22, we may modify the detector design to a pure kV & filter switched system. We have successfully interfaced PC based control electronics to the Toshiba constant potential generator in the laboratory, and should therefore be able to demonstrate very rapid kV switching. Filters (and the flip mirror) will be moved using stepping motors, which are also under computer control in the lab. The compression used in mammography acts as an immobilization as well, and therefore total exposures on the order of 2 seconds would not suffer motion in most cases.

The general diagnostic x-ray system is needed, because the high kV component of the dual energy acquisition far exceeds the kV capabilities of a dedicated mammography system. However, the 50 kV minimum on our Toshiba system requires compromise in the other direction; that is, 50 kV is probably not low enough. The spectra from this system were characterized as described previously¹⁵, and the effective energy with no added filtration at 50 kV was computed to be 27.4 keV. A computer simulation using only one type of elemental filtration showed that, at least for a single composition beam filter, the effective energy could not be appreciably reduced. For a silver ($Z=47$) filter, the effective energy of the beam could be reduced to 26.5 keV. We know from previous work^{9,10} that the optimal low energy beam should have an effective energy of around 19 to 20 keV. To address this, we plan to study the effect of using multiple elemental filters to "soften" the beam. Another realistic constraint is that the total attenuation cannot be unrealistic for tube-loading considerations. As an alternate to using stacked filters, we may install another x-ray tube on the system. The current x-ray tube is a high capacity (800,000 Heat Unit) angiography tube, which due to its high capacity has a fairly thick

aluminum tube port. A regular diagnostic tube may produce a softer x-ray beam. Also, we may explore with the Toshiba service personal if it is possible to reduce the low end kV of the generator.

6.4 Monte Carlo Modeling

The PI has reasonable experience with Monte Carlo modeling^{1,10,16-20}, but felt the need to re-evaluate the entire process, with the intent to update input parameters and reassess the accuracy of certain calculations. For example, the development of a new set of attenuation coefficients for all elements²¹ as initiated for this project, and the development of the TASMIP spectral models^{15,22} were both efforts to modernize and make more accurate the Monte Carlo results from our laboratory. In addition, our previous Monte Carlo code used in the past employed water as the scattering media. We modified the code so that the scattering media could be selected from any combination of glandular or fatty tissue (e.g. we can select 100% glandular, 100% fatty, 50%/50%, and so on). This required the development of new sets of form factors for the additional elements which are constituents of tissue (in addition to H and O, C, N, and P were added), as discussed in the literature^{23,24}.

While in this brief report a complete discussion of the Monte Carlo method will be avoided, one central issue with respect to the Monte Carlo algorithm itself will be mentioned. Single scatter Monte Carlo calculations are easy to perform, because the scattering angles θ and ϕ of the Rayleigh and Compton scattering events (Figure 23) can be calculated in the laboratory frame of reference. Multiple scattering effects, however, require coordinate transforms to get back to the laboratory frame, which in turn is necessary to determine interaction position¹⁹ and thus dose deposition. A new coordinate transform was developed recently by the PI, which was felt to yield a more straightforward solution. Figure 24 shows a multiply scattered x-ray photon in the laboratory frame. However, in the Monte Carlo procedure, the scattering angles θ and ϕ are determined along the trajectory of the photon ("photon frame"), as shown in Figure 23. A transform operator was recently derived as part of this project which allows the *direct* transformation of the photon frame coordinate system (where the photon is scattered at $(x=0, y=0, z=0)$ and is traveling along the positive z axis) back to the laboratory reference frame. This transform is given by:

$$\begin{vmatrix} \delta X \\ \delta Y \\ \delta Z \end{vmatrix} = \begin{vmatrix} -\Delta X \Delta Y & -\Delta Z & \Delta Z \\ \Delta X^2 + \Delta Z^2 & 0 & \Delta Y \\ -\Delta Z \Delta Y & \Delta Z & \Delta Z \end{vmatrix} \begin{vmatrix} X' \\ Y' \\ Z' \end{vmatrix}$$

The 3 x 3 matrix is normalized (divided by) by the quantity $(\Delta x^2 + \Delta z^2)^{1/2}$. So, once the scattering parameters of θ (0° to 180°), ϕ (0° to 360°), and r (distance to next interaction event) are calculated in the Monte Carlo program (by sampling the appropriate probability density functions for these parameters), the input vector values are calculated as:

$$\begin{aligned} X' &= r \sin(\theta) \cos(\phi) \\ Y' &= r \sin(\theta) \sin(\phi) \\ Z' &= r \cos(\theta) \end{aligned}$$

In the Laboratory Frame, the last two interaction locations, (x_1, y_1, z_1) and (x_2, y_2, z_2) are known, and the values in the transform matrix are determined by:

$$\begin{aligned}\Delta x &= x_2 - x_1 \\ \Delta y &= y_2 - y_1 \\ \Delta z &= z_2 - z_1\end{aligned}$$

The initial primary photon trajectory is easily defined by placing (x_1, y_1, z_1) at the focal spot and (x_2, y_2, z_2) at the entrant surface of the object (breast). The transform operator is applied to the input vector, and the resulting values of δx , δy and δz are calculated. These values represent the shift coordinates in the laboratory frame, which describe the location of the next x-ray interaction. For example,

$$\begin{aligned}x_3 &= x_2 + \delta x \\ y_3 &= y_2 + \delta y \\ z_3 &= z_2 + \delta z\end{aligned}$$

We feel that this more rigorous approach is an improvement to our previous technique, which involved having to go through a series of N-1 rotational transforms for the Nth interaction. This made it time-consuming to calculate the coordinates of significantly multiply-scattered photons (for example, the 10th scattering event for a photon would have to be run through a series of 9 coordinate transforms to determine laboratory coordinates¹⁹). This new approach also eliminates the need to calculate cosines (trigonometric functions are numerically intensive to compute), which most Monte Carlo routines make use of. The coordinate transform described above was thoroughly tested in many different ways to determine that it in fact does work. An geometric example of one of these tests is shown in Figure 25.

6.5 Monte Carlo Analysis of DgN

The first step in the Monte Carlo analysis, and one of its principal purposes, is to evaluate the dose to the breast for a given x-ray technique (kV, filtration, entrance exposure). Of course there are tables for the standard "roentgen to rad" conversion factors, called Dg_N values in mammography (normalized glandular dose), however these are available^{23,24} for standard clinical mammography x-ray beams only. It is necessary to evaluate the dose to the breast for very high energies (e.g. 120 kV) for the high energy component of the dual energy process.

Our Monte Carlo procedure was run using monoenergetic photon beams (10 million photons per keV per breast thickness). The Dg_N values were then calculated by prorating the monoenergetic results for the entrance x-ray spectrum in question. X-ray spectra were matched to the HVLs of Wu, Barnes and Tucker's data²³ by adding plastic to the beam (identical to what they did). Of course the Dg_N values are dependent on the thickness of the breast as well. We have attempted to repeat the work of Wu, Barnes and Tucker (WBT)^{23,24}, in an attempt to verify the accuracy of our Monte Carlo procedure. We have gone through and evaluated most aspects of the code, and as one example, the attenuation coefficients we used were compared against Hammerstein²⁵ (Figure 26), with excellent results.

The Dg_N values calculated using our code ("this work") are compared against the published values of Wu, Barnes and Tucker (WBT), and are shown in Figures 27 and 28. We have been

disappointed by the poor level of agreement, which is not adequate as these figures indicate. The PI has spent the past 3 (frustrating) months trying to rectify these differences. Unfortunately, the WBT paper was published in a clinical journal where technical detail is sometimes compromised for the sake of clarity and brevity. In our case, we are thwarted to some extent by not knowing all the technical parameters that went into the WBT calculations. We have contacted Wu, Barnes, and Tucker, for greater details on their study, however due to extensive travel and serious illness of these esteemed colleagues, we have yet to have an opportunity to fully discuss their results. A more direct way to compare our results to those of others is to examine the monoenergetic dose results. Comparing the monoenergetic results is a better comparison since they are not obscured by the additional complexity of the x-ray spectra used. We intend to make these comparisons with Dr. Gary Barnes once he has a chance to meet with the PI.

The D_{gN} values of Wu, Barnes and Tucker were based significantly on the experimental work of Hammerstein²⁵, which dates back to 1979, prior to, for example, the common usage of molybdenum anode x-ray systems. In realizing that Monte Carlo techniques need to be verified against real data, we have made the decision to completely validate our Monte Carlo code experimentally. Initial experiments have been made to date. We are using sheets of film (Kodak therapy localization film, x-omat TL) interleaved with commercially available BR12 material (CIRS). Film is a reasonably accurate dosimeter, if certain effects are corrected for. As an example of this work, the H & D curves for the TL film are shown for 3 different beam energies in Figure 29. The film response demonstrates only a slight dependence on beam energy. The film images were digitized using a Lumisys 150 laser digitizer, and a relationship between digital number and x-ray exposure was established (Figure 30). This relationship was fit to an analytical equation (TableCurve 2D), which allows other digitized films to be converted into units of exposure. This is our basic approach, however, it is necessary at these low x-ray energies to correct for the influence of the layer of silver halide in the x-ray propagation. This effort has just begun, but as an example of how experimental results may relate to the Monte Carlo simulations, Figure 31 shows the distribution of exposure over the 24 cm x 30 cm field of view of a typical mammography system (in this case, the 500T in our research lab). The heel effect was not considered in previous Monte Carlo studies, that we are aware of.

Using our Monte Carlo routine as it stands, prior to full experimental validation, a series of output was calculated. Figure 32 illustrates the angle and energy distribution of the x-ray photon distribution exiting a 4 cm glandular breast, from a 30 keV normally incident x-ray beam. This two dimensional histogram is presented as an isometric plot. Another similar plot is shown in Figure 33, where a 100 keV x-ray beam was incident upon a 4 cm breast. A total of 10^8 photons were input for each case (at each keV). Figure 33 shows a ridge which as the angle increases, the energy corresponding to the ridge decreases. This is of course the effect of scattered photons losing more energy when scattered through larger angles. The distributions in Figures 32 and 33 show single and multiple scattering events. The scalloping (the appearance of multiple peaks) on these figures is an artifactual result of the discrete binning onto the grid. The 2-D data shown in these figures was calculated for different patient thicknesses (3, 4, 5, 6, 7, and 8 cm) and from 2 keV to 140 keV by 1 keV intervals. Thus, by knowing the incident spectrum for a given breast thickness, the scattered energy versus angle distribution can be appropriately weighted, to get the polyenergetic version of these plots. These plots describe the scattered energy propagation through an imaging system, and the primary propagation is calculated using the scatter to primary results of these calculations (not shown) and standard Lambert-Beers equations.

The x-rays scattered from the breast in the forward direction (Figures 32 and 33) will next intersect with the anti-scatter grid in the imaging system. The energy and angle transmission

probabilities for two different grids are illustrated in Figures 34 and 35. Figure 34 shows the performance of a 12:1 carbon fiber interspaced grid, and Figure 35 shows the results for a 5:1 carbon fiber interspaced grid more commonly used in mammography. The scattered transmission (all transmission above 0°) is excessive for the 5:1 grid. The discontinuity at 88 keV is the result of the k-edge of the lead bars in the grid - above 88 keV scattered photons are better removed (transmission is less) because the linear attenuation coefficient abruptly increases at this energy for Pb. The polyenergetic angle versus energy data (similar to Figure 33) for a given patient thickness can be passed through a grid numerically by simply multiplying the two arrays (Figures 33 with Figure 34, for example). This approach, using table look-up, makes it numerically feasible to study many different permutations without having to actually compute each permutation using stochastic (Monte Carlo) methods. It is therefore a relatively simple matter to take the input x-ray spectrum, the scattering functions, the grid transmission functions, and the detector detection functions (not shown but easily calculated), and compute the "imaged" signal to noise ratio for a specific target (e.g. a small microcalcification). Taken with the dose (mrad), the figure of merit (FOM) of the SNR^2 / glandular dose can be calculated. This FOM is useful for optimizing the dose efficacy of various dual energy mammographic techniques. The code is in place already to perform the calculations described here, what needs to be done is the validation of the Monte Carlo results (as described above). Once validated, the calculation of the optimal techniques can proceed rapidly.

It is our intention to devote significant effort to fully verify our Monte Carlo results against experimentally determined data. The Monte Carlo studies are of fundamental importance towards determining glandular dose, scatter distribution exiting the patient towards the detector, the performance and optimization of the grid, and so on. Once completely verified, the rapid assessment of Tasks 1.1, 1.2, and 1.4 can be completed.

6.6 Scatter Suppression

Scatter suppression is a necessary component in dual energy imaging, because the biasing of the signal by scatter results in errors in the quantitation that is intrinsic to dual energy decomposition techniques. We have some experience with software techniques for scatter reduction^{26,27}, however our current thinking is that a hardware solution will in general be superior in most cases. Towards this goal, we have developed a relatively simple approach towards correcting for scatter in both the high and the low energy images.

A thick attenuating plate was drilled on 5 mm centers with ~ 0.20 mm holes (call this the "hole plate"). The full field dual energy image acquisition occurs as usual, and then it is (rapidly) repeated with exactly the same exposure conditions (kV, mAs and filtration), except with the "hole plate" in front of the object (breast). The amount of additional exposure due to this plate is the ratio of the open holes to the entire area, which we estimate to be an increase of $\sim 0.1\%$ radiation. Depending on the magnification and the focal spot size, the diameter of the holes may need to be slightly increased to avoid serious penumbra effects. It is an easy matter to automatically identify (using a computer) the areas of the otherwise dark image which correspond to the positions of the holes. These areas are identified, and the measurement of the peak gray scale in these areas is an estimate of the primary radiation reaching the detector system at that point. By going to the corresponding (high energy or low energy) image that was taken without the hole plate, an assessment of the scatter and the primary is made, and by subtraction the amount of scatter at each hole location can be determined. Since scatter is a low frequency phenomenon, the scatter measurements taken every 5 mm in the image can be

interpolated using cubic spline, polynomial, or other interpolation techniques. The bias due to the scatter in the image is then removed by subtraction, for both the low and high energy images.

6.7 Dual Energy Imaging

Dual energy images were acquired using a 50 kV unfiltered x-ray beam and a 100 kV beam with 4 mm of added filtration. We have not yet developed a reasonable dual energy phantom for this work, and for the purposes of demonstration we used a simple Lego phantom. The Lego phantom has a lot of intrinsic subject contrast (~anatomical noise) and therefore illustrates the role that dual energy mammography may play. Figure 36 illustrates the low energy (50 kV) image of the Lego phantom, which was comprised of some Lego bricks, an additional 2 cm of BR12, and some tie-wraps for added "clutter". The high energy image of the phantom is just a lower contrast version of Figure 36. Dual energy subtraction methods were used to produce Figure 37. The two calcifications (chips from a seashell, a micro-calcification test tool recommended by Dr. Carolyn Kimme-Smith at UCLA*) are quite visible in the dual energy subtraction image, whereas they are not plainly visible in the single energy conventional image. We found that one of the Lego bricks also was enhanced on the dual energy image (Figure 37), and we suspect that this is a 35 year old Lego brick (from the PI's youth) which is composed of a different, higher-Z red pigment than the other, newer Lego bricks (owned by the PI's young son). Certainly not a major scientific discovery, but is an interesting example of serendipity.

The dual energy image, $DE(x,y)$, shown in Figure 37 was calculated as:

$$DE(x,y) = LN[I_{HI}(x,y)] - R \times LN[I_{LO}(x,y)] \quad \text{Equation 1}$$

Where I_{HI} was the high energy image and I_{LO} was the low energy image. There is much discussion in the literature concerning the most viable algorithm for dual energy subtraction, and of course the selection of the algorithm will have a profound influence on the quality of the subtracted image. We are pursuing an analysis of different algorithms. Computer simulations were used to study the following algorithms to date:

$$\text{ALG-1} \quad DE(x,y) = a + b \times LN[I_{HI}(x,y)] + c \times LN[I_{LO}(x,y)]$$

$$\text{ALG-2} \quad DE(x,y) = a + b \times LN[I_{HI}(x,y)] + c \times LN[I_{LO}(x,y)] + d \times (LN[I_{HI}(x,y)])^2 + e \times (LN[I_{LO}(x,y)])^2$$

$$\text{ALG-3} \quad DE(x,y) = a + b \times LN[I_{HI}(x,y)] + c \times LN[I_{LO}(x,y)] + d \times (LN[I_{HI}(x,y)] \times LN[I_{LO}(x,y)])$$

$$\text{ALG-4} \quad DE(x,y) = a + b \times LN[I_{HI}(x,y)] + c \times LN[I_{LO}(x,y)] + d \times (LN[I_{HI}(x,y)])^2 + e \times (LN[I_{LO}(x,y)])^2 + f \times (LN[I_{HI}(x,y)] \times LN[I_{LO}(x,y)])$$

Notice that because the dual energy subtracted image $DE(x,y)$ is rescaled for display, Equation 1 is numerically identical to Algorithm 1. These four algorithms are found commonly in the literature. However, the results of our computer simulations, which used a set of 2000 pixels (spanning the

* Personal Communication

different thickness combinations) to solve for the coefficients a, b, c....using multiple regression analysis techniques, indicated that Algorithms 2, 3 and 4 were not statistically better than the basic linear equation given by Algorithm 1. These results were for a noiseless simulation.

The computer simulations made use of a 50 kV unfiltered tungsten beam and a separate 120 kV, aluminum filtered beam, with one Lanex screen as a detector ($60 \text{ mg/cm}^2 \text{ Gd}_2\text{O}_2\text{S:Tb}$). Step wedges composed of Lucite (0 to 40 mm Lucite) and of aluminum (0 to 1.6 mm Al) were simulated and imaged with the Lucite step wedge orthogonal to the aluminum one. The multiple regression (single value decomposition) solution to the coefficients (in Algorithm 1) for an aluminum image yielded $a = -16.84$, $b = -0.522$, and $c = 0.8325$. While the other algorithms were not capable of significantly outperforming algorithm 1, there is a substantial error residue when the dual energy decomposed "aluminum" image is compared with the actual aluminum thickness template that was "imaged" in this simulation. Therefore, we are studying the potential of other algorithms for producing accurate dual energy subtracted images. This is being pursued in the simulation environment because the variables can be controlled precisely (e.g. initially we have studied the scatter-free and noise-free situation, and we can start adding scatter and quantum noise into the images to study how these factors affect image quality).

The computer simulations described above were performed using equations which describe the physics of image acquisition, for example the low energy image is generated by:

$$I_{LO}(x,y) = \frac{\int \Phi_{LO}(E) D(E) E dE}{\int \Phi_{LO}(E) D(E) \text{ EXP}[-\mu_1(x,y,E) t_1(x,y) - \mu_2(x,y,E) t_2(x,y)] E dE},$$

where $\Phi_{LO}(E)$ is the x-ray fluence, $D(E)$ is the detector response, the subscript 1 refers to material 1 (e.g. Lucite or tissue), subscript 2 refers to material 2 (e.g. aluminum or calcifications), μ is the attenuation coefficient and t is the thickness. A similar equation describes the high energy acquisition, substituting the high energy x-ray beam, $\Phi_{HI}(E)$, for the low energy one, $\Phi_{LO}(E)$. These equations include the influence of beam hardening, since they integrate the spectrum. We are currently exploring iterative reconstruction techniques where equations such as the one above are using in an iterative manner, iterating on t_1 and t_2 in search of the measured values of $I_{LO}(x,y)$ and $I_{HI}(x,y)$, having characterized the spectra $\Phi_{LO}(E)$ and $\Phi_{HI}(E)$, and knowing μ_1 and μ_2 from tables. Iterative solutions often have better immunity from noise, and can correct for other influences (not indicated analytically) such as x-ray scatter. The iterative solution can be performed using table lookup, by pre-computing over all reasonable ranges of t_1 and t_2 (once).

Computer simulations in combination with data acquired from the dual energy mammography system in our laboratory will be used to study dual energy algorithms. The influence that inhomogeneous breasts (e.g. 50% glandular, 50% fatty) have on the subtraction of tissue will also be studied.

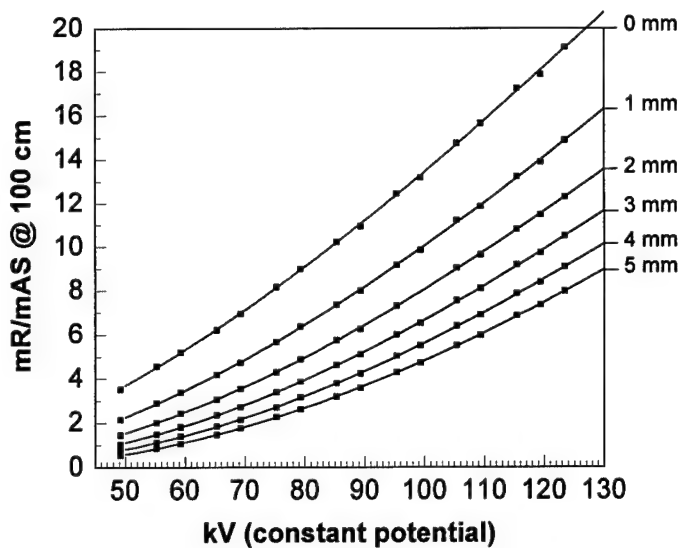


Figure 1.

The x-ray output of a general diagnostic x-ray system in the P.I.'s laboratory is shown as a function of kV. The output for different amounts of aluminum filtration (0 mm - 5 mm) is illustrated. The solid symbols represent measure data points, and the corresponding curves were generated using commercially available curve fitting software.

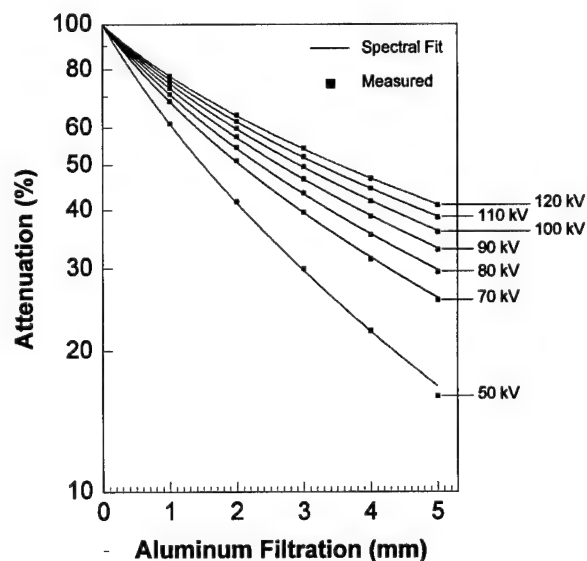


Figure 2.

The attenuation curves as a function of aluminum filtration are illustrated at a variety of kVs. These data are representative of the beam *quality*, while the data in Figure 1 describe the beam *quantity*.

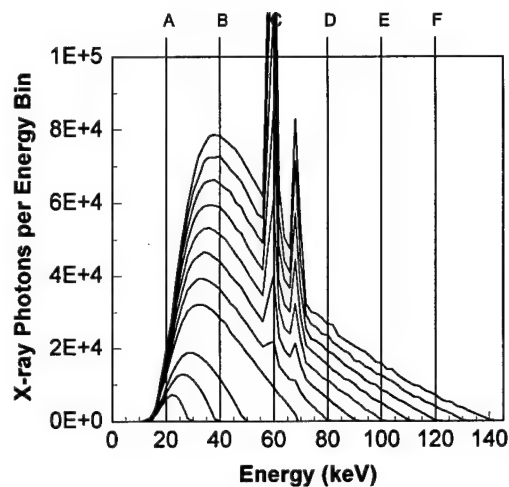


Figure 3.

A total of 11 x-ray spectra are illustrated. These spectra were slightly modified (by the mathematical addition of aluminum filtration) from the tabulated Fewell spectral data. The spectra as shown match the output characteristics (mR/mAs and attenuation profiles) of the x-ray system in the P.I.'s laboratory. The vertical lines illustrate the direction in which the spectral data are interpolated. For example, the vertical line labeled B corresponds to the same data labeled B shown in Figure 4. Alternate representations of the data along each vertical line are shown for lines A through C in Figure 4, and lines D, E, and F are shown in Figure 5.

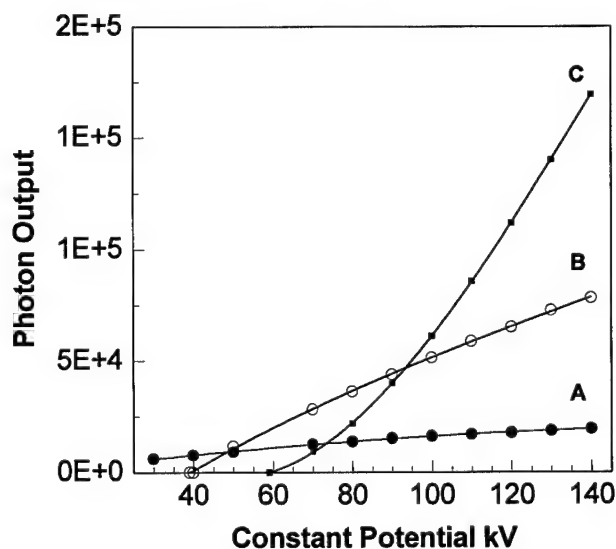


Figure 4.

The solid data points shown in this figure are the same data as illustrated in Figure 3, albeit plotted on different axes. The curves (solid lines) shown in this figure were produced with interpolating polynomials. The three different curves correspond to different energy bins in the parent spectra, where A = 20 keV, B = 40 keV, and C = 60 keV. As the kV across the x-ray tube is increased, the fluence at a given energy also increases, and that is what is illustrated in this plot.

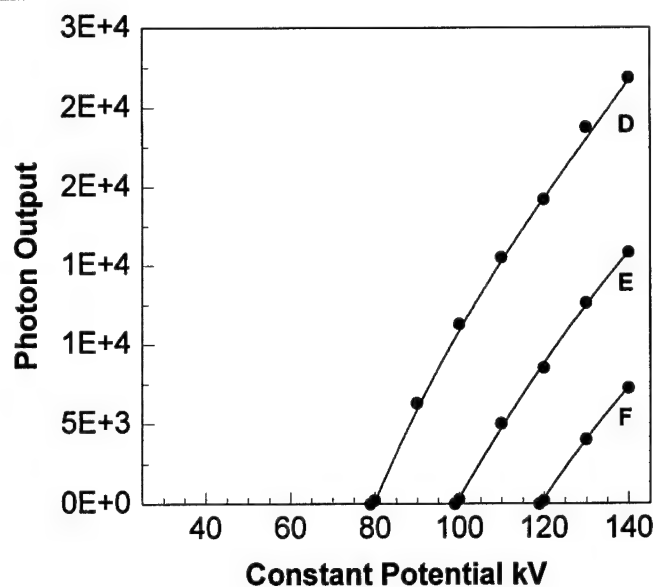


Figure 5.

This figure shows the raw data plus the interpolated curves for three energies shown in Figure 3, where D = 80 keV, E = 100 keV, and F = 120 keV.

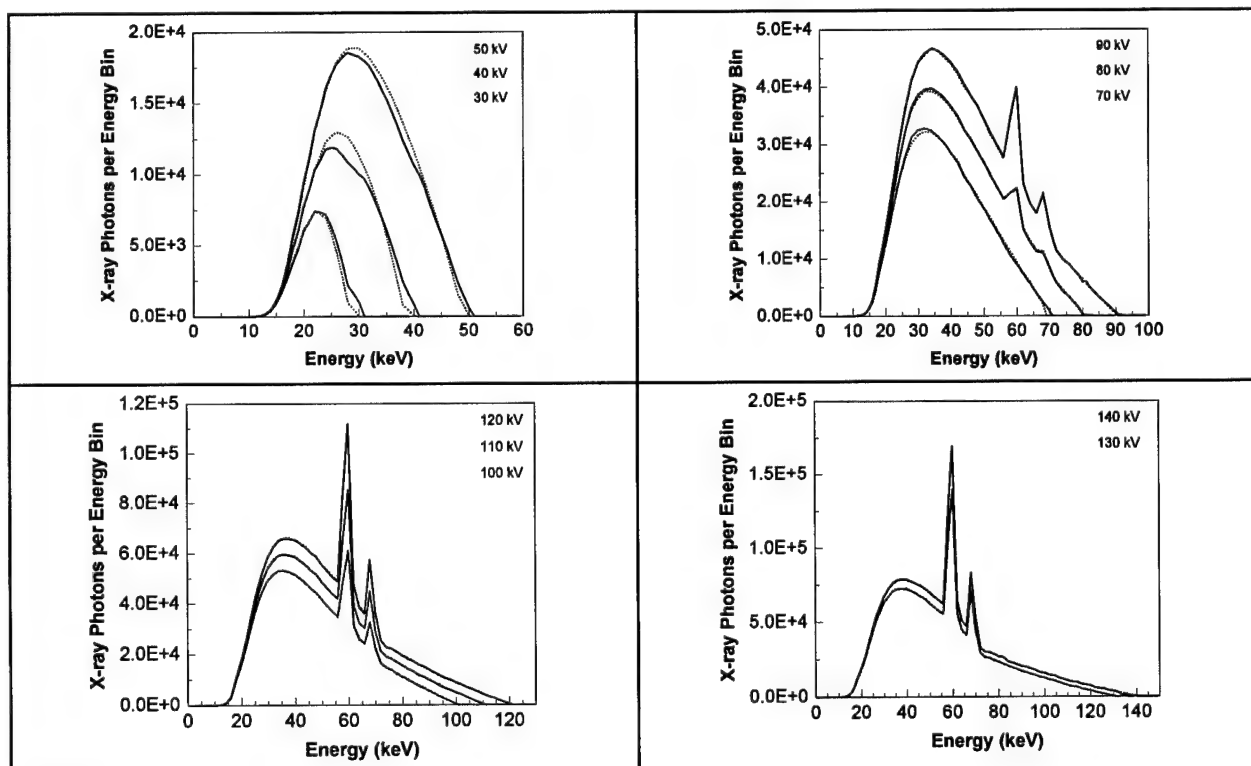


Figure 6.

In these four figures a total of 11 x-ray spectra are compared. The dotted lines correspond to the x-ray spectra produced by the TASMIP model, while the solid lines correspond to the original Fewell tabulated spectra. Excellent correspondence between the model and actual spectra is observed. However, in Figure 6a showing the 30, 40 and 50 kV spectra, some amount of deviation is observed. This is because the experimentally measured spectra at these three kVs were measured with a single phase generator, while the modeled spectra assumed a constant potential generator.

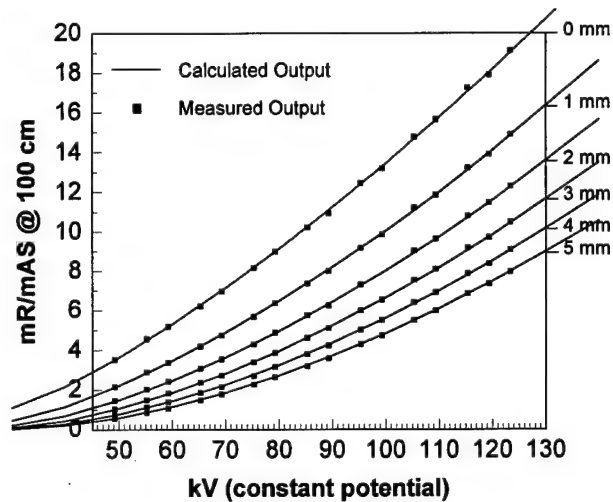


Figure 7.

The output of the x-ray system in the P.I.'s laboratory is a function of kV. The solid data points were measured values from the laboratory, and these values are identical to those shown in Figure 1. However, the curves shown in this figure were generated from the TASMIP spectral model. The spectral model is capable of both matching the *quantity* and *quality* of the x-ray system in the P.I.'s laboratory.

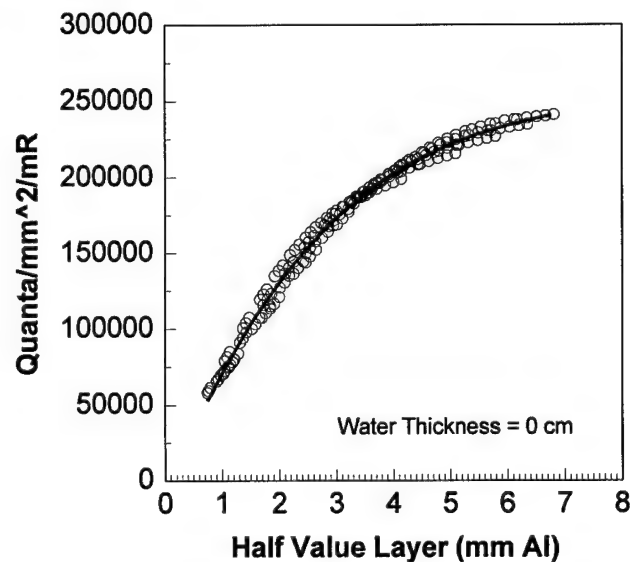


Figure 8.

The x-ray quantum fluence per mR is illustrated as a function of half-value layer (HVL). There was no object in the beam. The spectral model was used to create x-ray spectra with different kVs, different amounts of aluminum filtration, and different amounts of kV ripple. It was found that the fluence per mR tracked reasonably well with the half-value layer calculated for the spectrum, as shown in this plot.

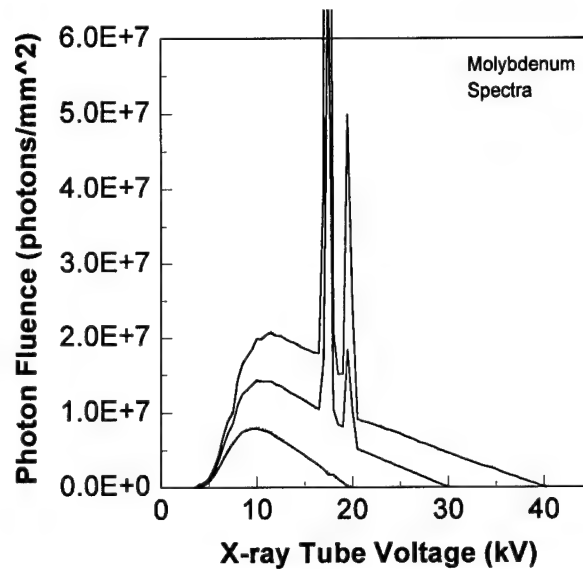


Figure 9.

The TASMIP model for the x-ray mammography systems are shown, for 20, 30, and 40 kV. The model spectra are illustrated using dotted lines, however due to the excellent fit the overlying measured x-ray spectra from Fewell (shown as a solid line) obscures the dotted line.

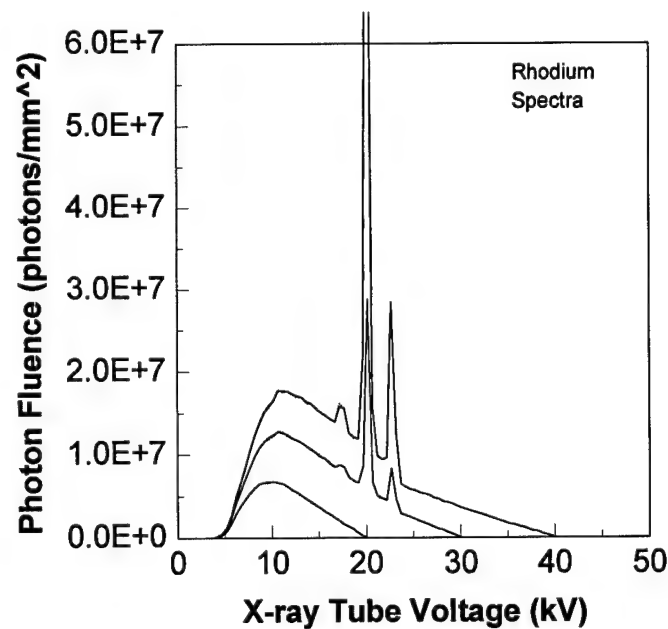


Figure 10.

The modeled and experimental spectra for a rhodium anode x-ray mammography system. Again, the modeled spectra (dotted lines) are obscured by the experimental spectra (solid lines), due to the excellent match between each spectra.

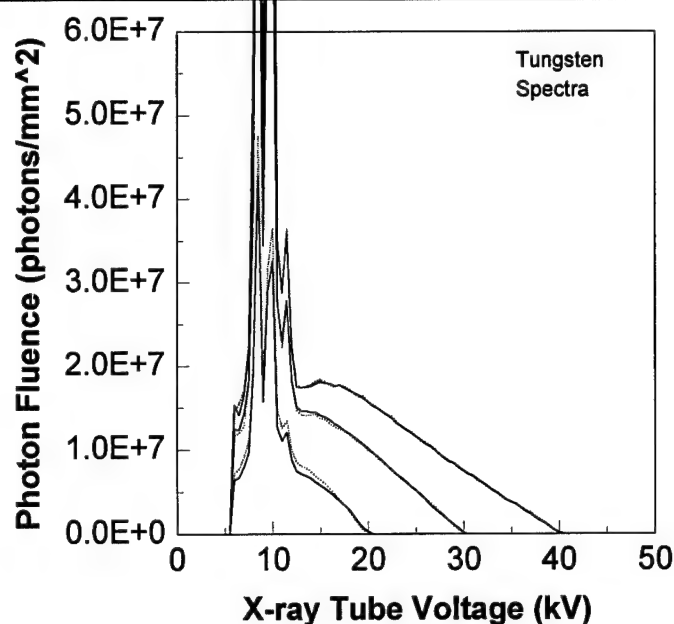


Figure 11.

The modeled spectra (dotted line) is shown along with the experimentally determined spectra (solid line), for a tungsten anode in the x-ray mammography energy region. A large number of L emission edges are observed in the 8 keV region of the spectrum.

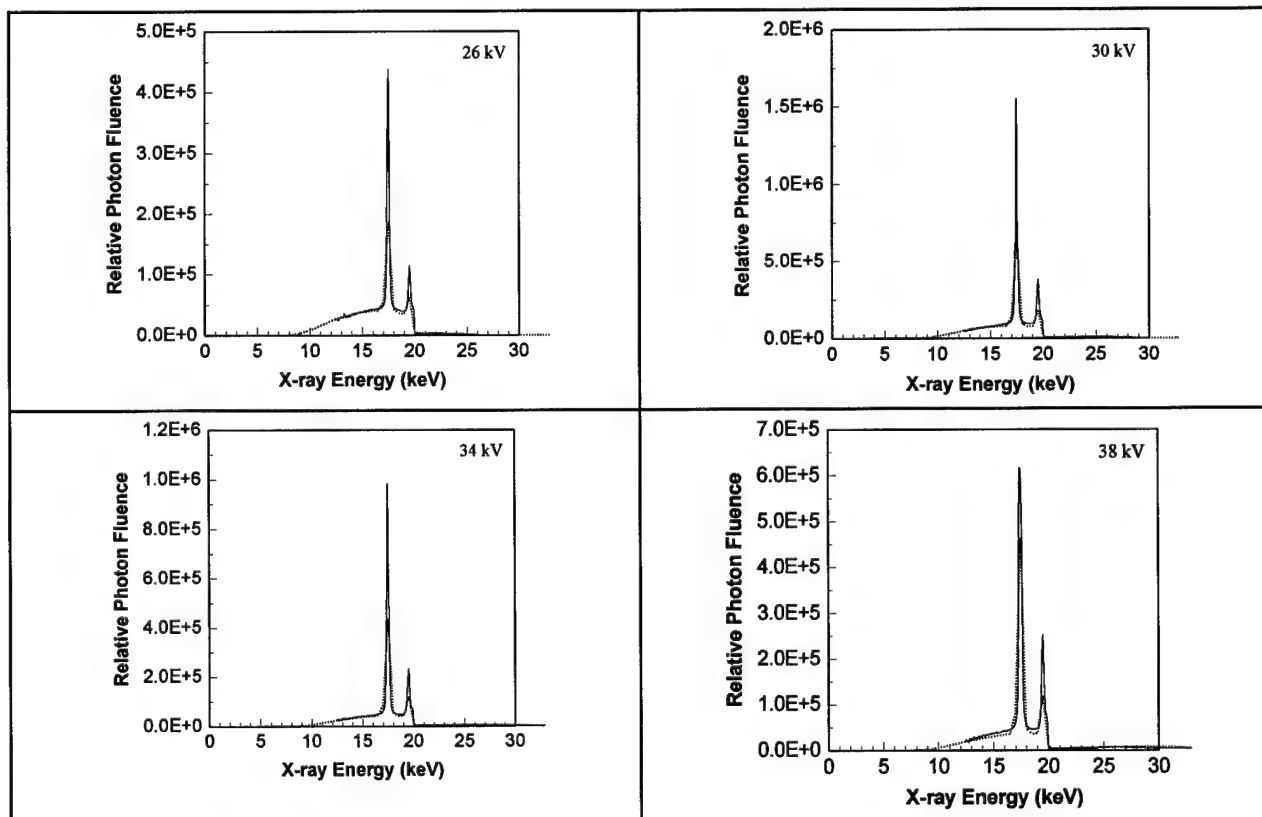
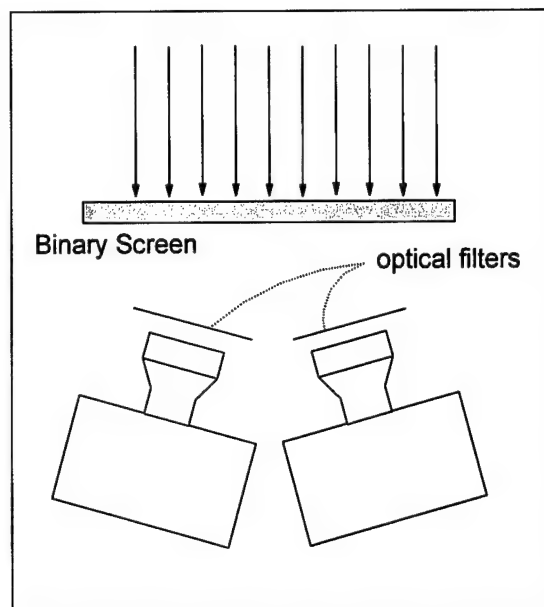


Figure 12.

The x-ray spectrometer was used to measure the x-ray specter output of a GE 600T x-ray mammography system in our clinic. These measured spectra are compared with the mathematically filtered (30 microns of Mo) tabulated Fewell spectra. Four spectra are compared, at 26, 30, 34, and 38 kV. An excellent match is seen between the measured spectra and the data tabulated by Fewell.



original design using binary screen

Figure 13.

The original design for the dual energy mammography system for this grant was to use a binary screen. A binary screen is an intensifying screen composed of green-emitting $\text{GD}_2\text{O}_2\text{S}$ and red-emitting $\text{Y}_2\text{O}_2\text{S}$. The gadolinium phosphor absorbs preferentially the higher energy x-ray photons in the incident polychromatic spectrum, while the yttrium phosphor absorbs preferentially the lower energy photons due to the relative placement of their K edges. Two CCD cameras with optical filters (red and green) are used to image the light emission from the binary screen. This system is essentially a two channel (low energy, high energy) dual energy imaging system. While the energy separation performance of this system is good, it was concluded that better energy separation can be achieved using a pulsed x-ray system using two incident x-ray spectra. Therefore, the binary screen based dual energy mammography system was abandoned in search of a system with the potential for maximum signal to noise ratio.

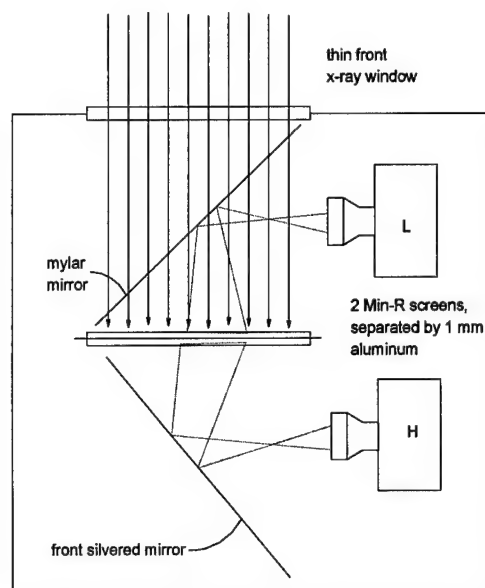


Figure 14.

The system shown schematically represents the evolution of the dual energy mammography system in our laboratory. A sandwich screen system is seen in the center of the schematic, and the light given off from the front, low energy intensifying screen is reflected off a very thin mylar mirror and captured by the upper camera (marked L). The high energy, aft screen produces light which is reflected off a front-silvered mirror and captured by the lower CCD camera (marked H).

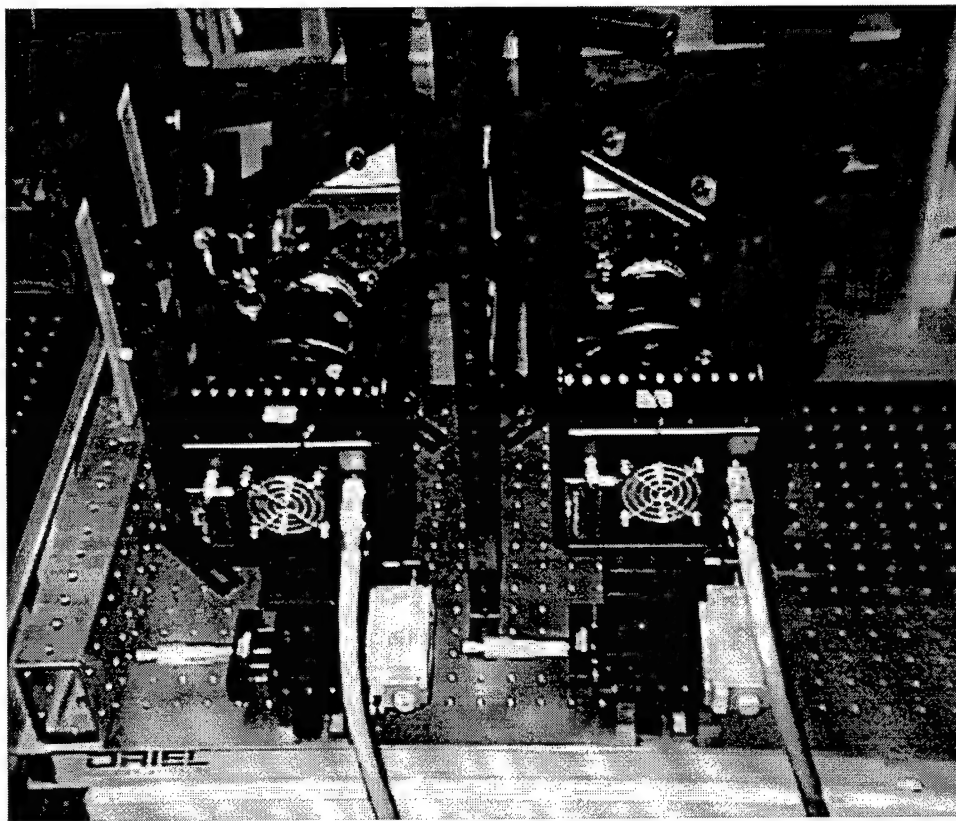


Figure 15.

A photograph of the dual energy mammography system in our laboratory. The two, 2048 x 2048 cooled 12 bit CCD cameras are seen in the foreground. The x-ray beam enters from the left side of the picture, passes through a very thin mylar mirror (seen on the left), and strikes a pair of intensifying screens (located behind the vertical post in the center of the picture). The light emitted from the front screen reflects off the mylar mirror (left) and is recorded by the CCD camera on the left of this picture. After switching to a much higher kV, a second pulse of x-rays produces light in the back screen, which is reflected off the mirror (right side of this picture), and is recorded on the CCD camera on the right. This dual energy mammography system configuration was characterized with the results presented in the following six figures.

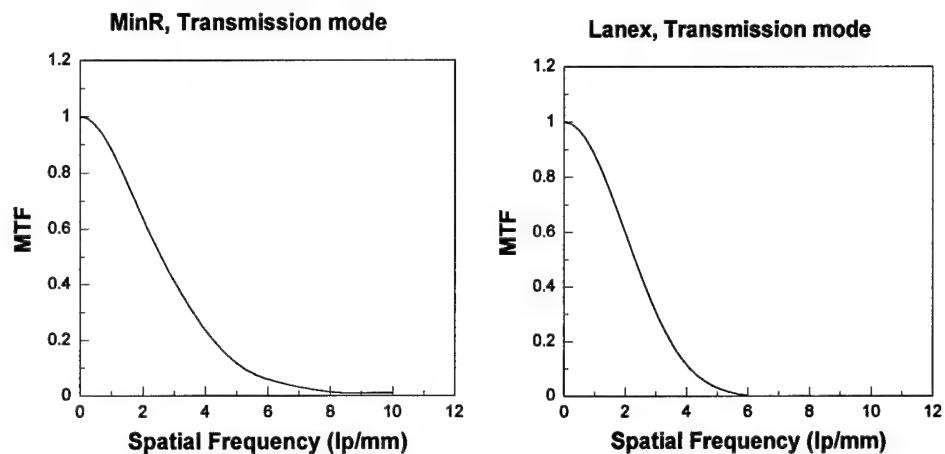


Figure 16.

The dual energy mammography system shown schematically in Figure 14 and pictorially in Figure 15, was tested in performance using both Min-R and Lanex intensifying screens (alternately). For the aft screen/optic/camera configuration, which is used in transmission mode, the MTF for the Min-R and Lanex screens are shown in this figure. As expected, the Min-R screen has slightly better spatial resolution.

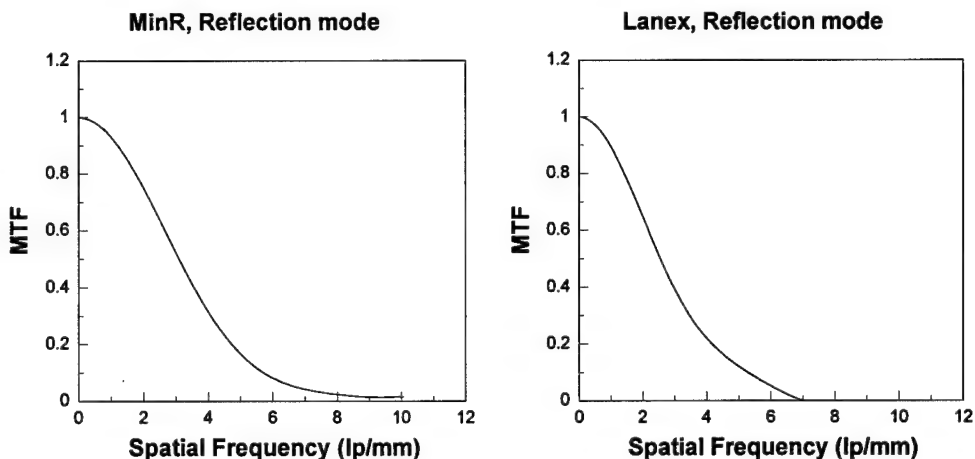


Figure 17.

The MTFs for the front screen/optic/camera configuration are shown. Here again, the Min-R screen produces slightly better spatial resolution than the thicker Lanex screen.

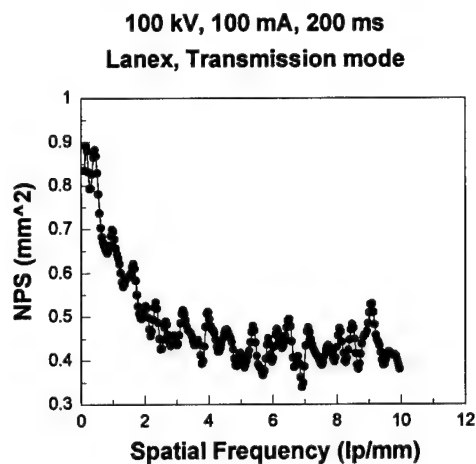
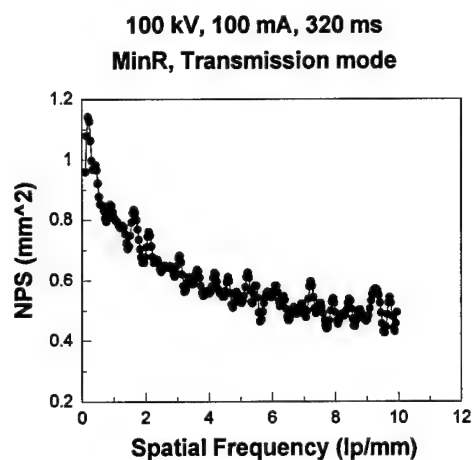


Figure 18.

The noise power spectra (NPS) are illustrated for both the Min-R and Lanex screens in transmission mode. The transmission mode camera is the high energy (aft) imaging system, and these measurements were made at 100 kV.

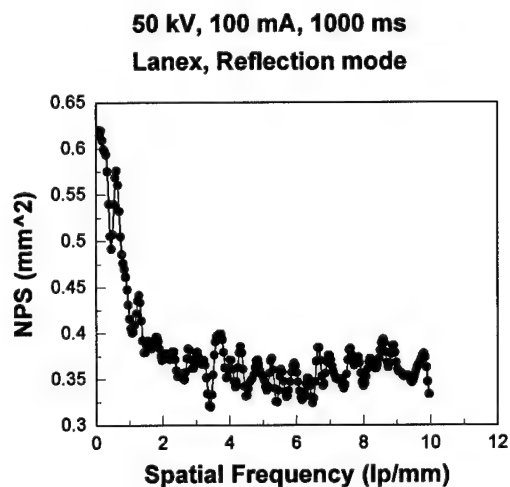
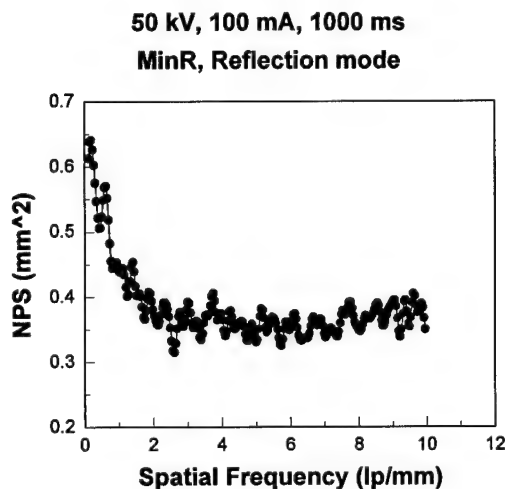


Figure 19.

The noise power spectra measured at 50 kV are illustrated for both the Min-R and Lanex screens in reflection mode.

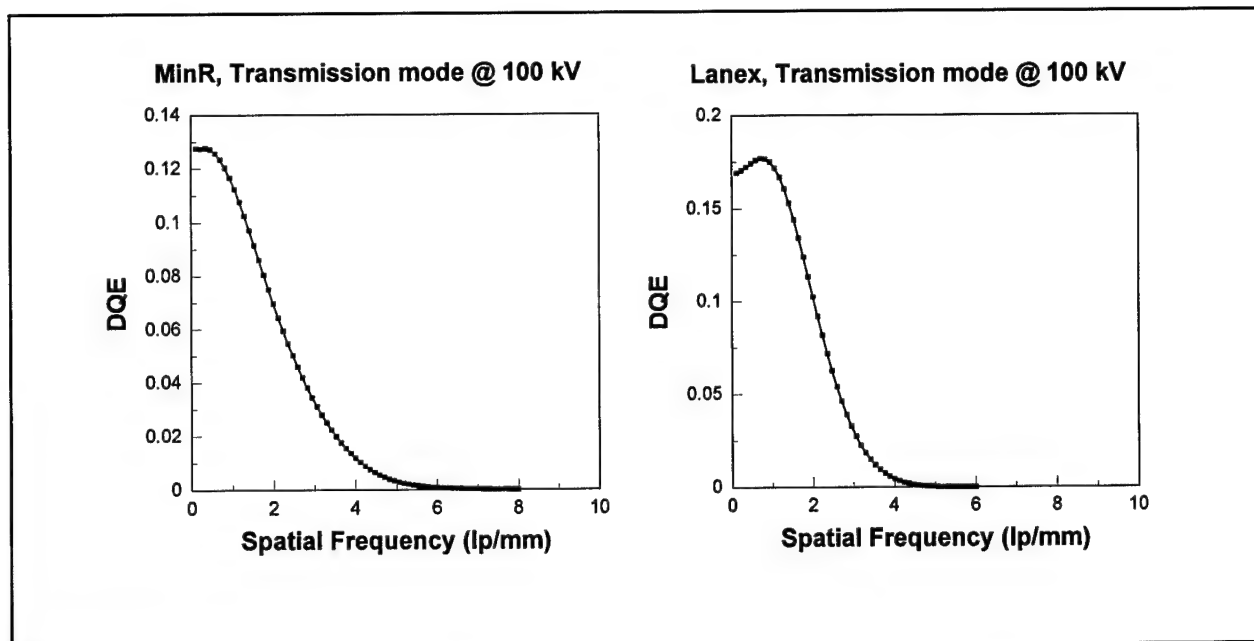


Figure 20. The detective quantum efficiency, $DQE(f)$, is illustrated in this figure for transmission mode imaging for both the Min-R and Lanex intensifying screens. Whereas the Min-R screen performance extends to slightly high frequencies than that of the Lanex screen, the zero frequency DQE of the Lanex screen is higher than that of the Min-R screen as expected. The NPS curves were smoothed prior to calculating the $DQE(f)$ from them. The smoothing may explain the peak observed at about 1 lp/mm.

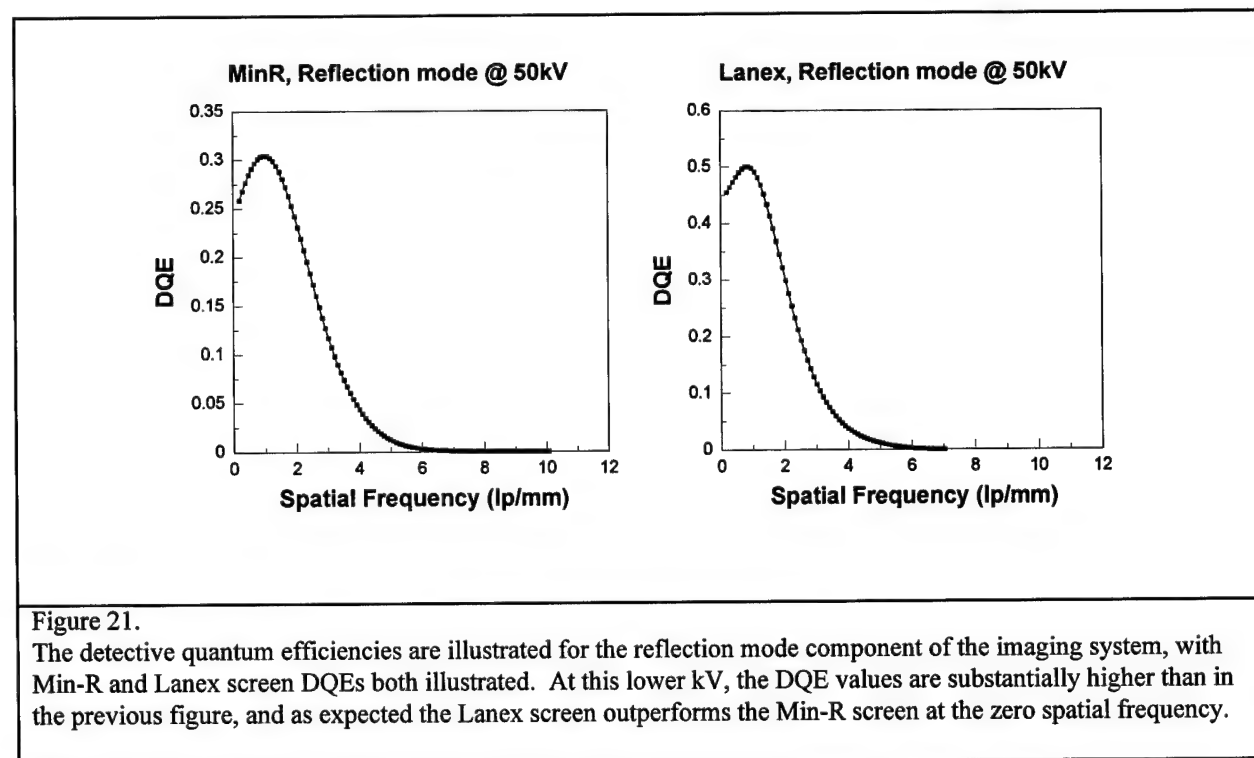


Figure 21. The detective quantum efficiencies are illustrated for the reflection mode component of the imaging system, with Min-R and Lanex screen DQEs both illustrated. At this lower kV, the DQE values are substantially higher than in the previous figure, and as expected the Lanex screen outperforms the Min-R screen at the zero spatial frequency.

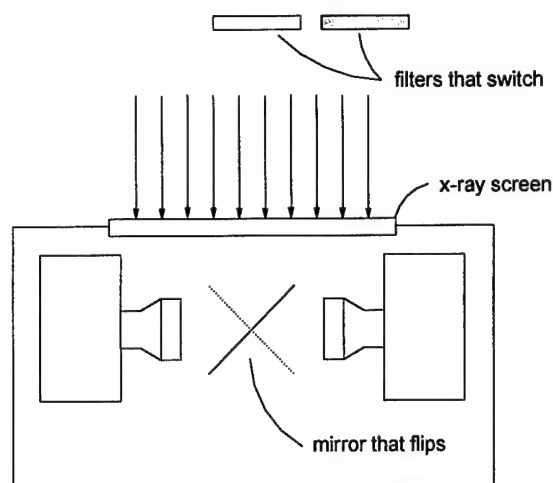


Figure 22.

The dual energy mammography system shown schematically in Figure 14 requires significant magnification of the object, resulting in some loss of spatial resolution due to focal spot blurring. Shown in this figure is the possible next evolution in our system design, which reduces the magnification factor significantly. Furthermore, instead of using a sandwiched detector, filters are used at the x-ray tube to spectrally harden or soften the x-ray beam in addition to kV switching. This system design requires only one intensifying screen. Because the read out time of these high resolution cameras is on the order of 30 seconds, two cameras are needed in order to acquire two pulsed kV images back to back in the subsecond time frame. A mirror which flips, and thereby shunts the light from the screen from one camera to the other is also required.

scattering reference coordinates

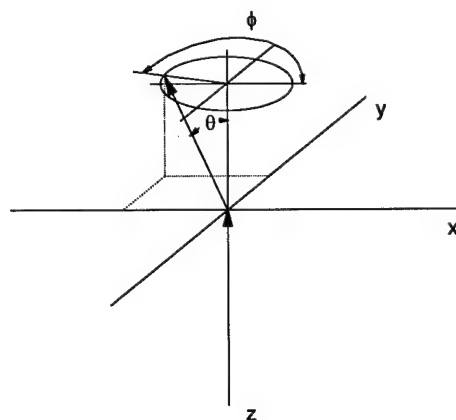


Figure 23.

The coordinate system for the "photon frame" is illustrated. This is the coordinate frame in which the angles θ and ϕ for Compton and Rayleigh scattering are defined. These angles are generated from the appropriate probability density functions using standard Monte Carlo techniques.

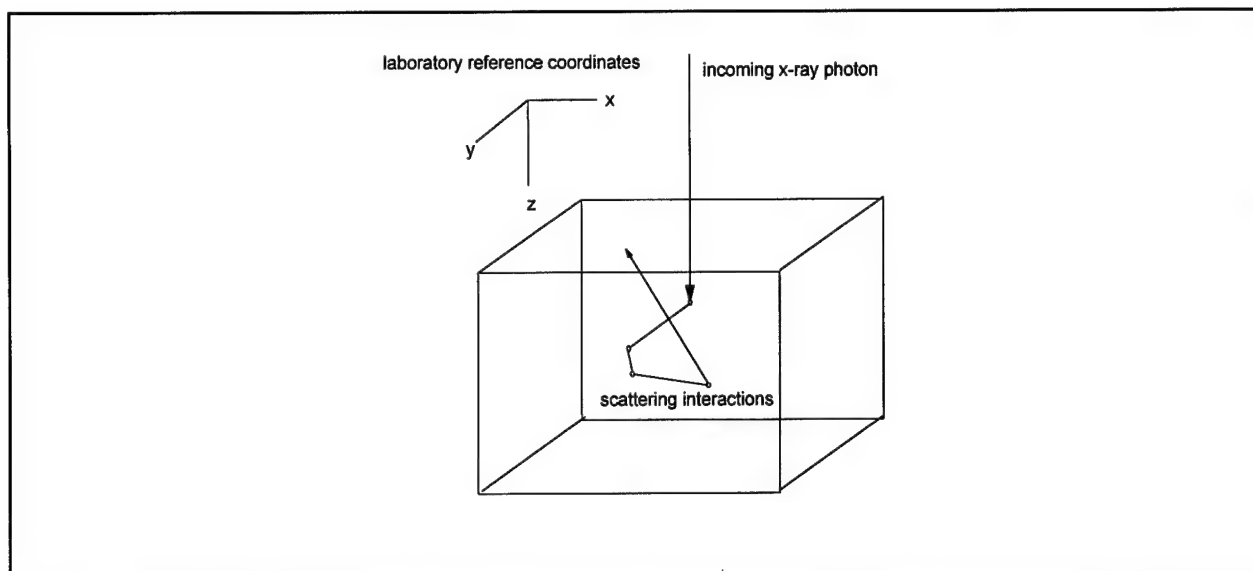


Figure 24.

This figure shows the laboratory reference coordinates. It is necessary to convert the photon frame coordinate system, illustrated in the previous figure, to the coordinate frame illustrated in this figure.

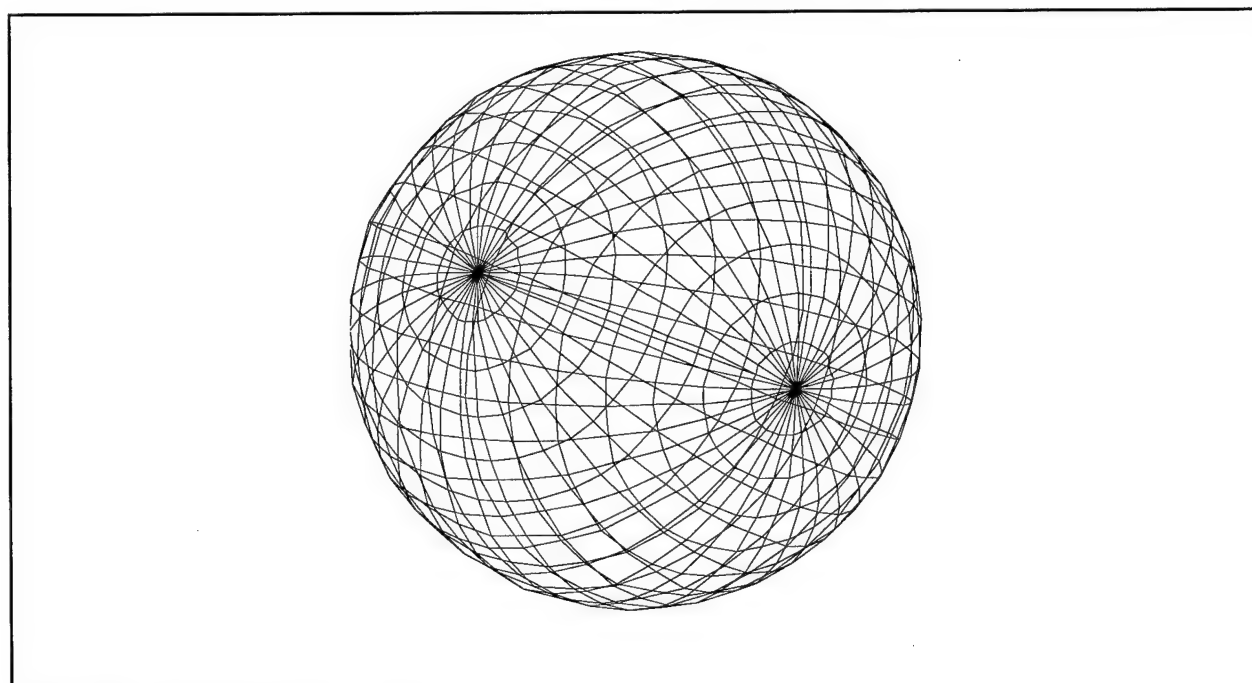


Figure 25.

This figure shows test results from the transform operator described in the text. The scattering foci is at the center of the "sphere", and the lines on the sphere were drawn by projecting the transformed coordinates onto an x-y plane. The test procedure calculated a series of projected radii at different angles, over θ and over ϕ (alternately). The ends of each radius were connected graphically. The result is analogous to drawing lines of latitude and longitude on a globe.

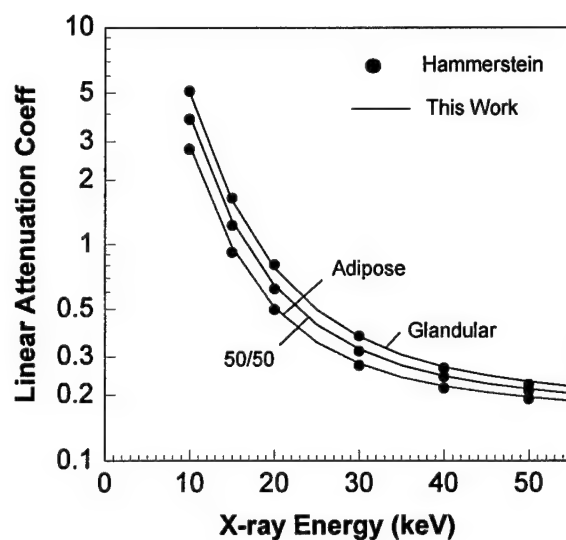


Figure 26.

The linear attenuation coefficients for differing types of breast tissue are compared. The Hammerstein data are shown as symbols, while the attenuation coefficients used in our work are illustrated as solid lines. Excellent agreement between these data is observed.

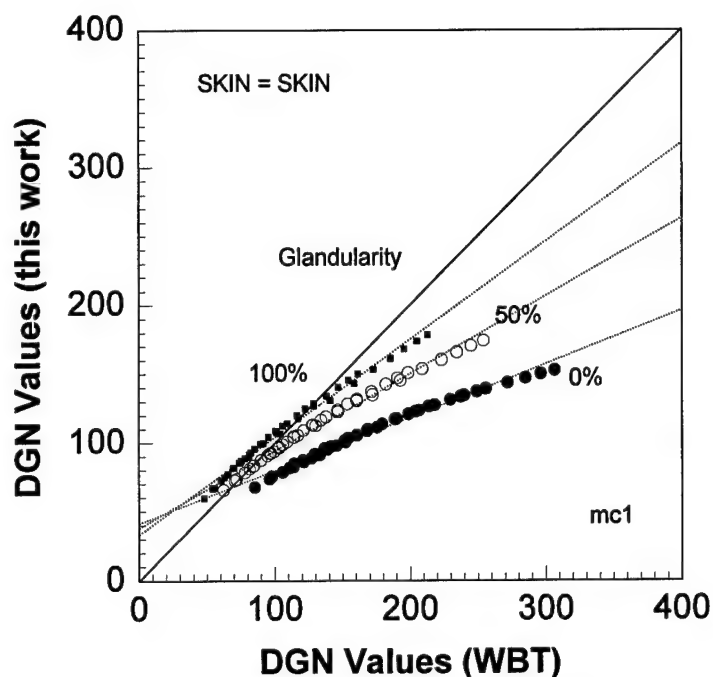


Figure 27.

The normalized glandular dose (DGN) of this work are compared against the DGN values of Wu, Barnes, and Tucker (WBT). The DGN values for three different glandularities (0%, 50%, 100%) are illustrated. These results were obtained using the assumption that the skin thickness and composition as given by Hammerstein were used. The points for each kind of glandular are for 3, 4, 5, 6, 7 and 8 cm of tissue at kVs ranging from 23 to 35 kV.

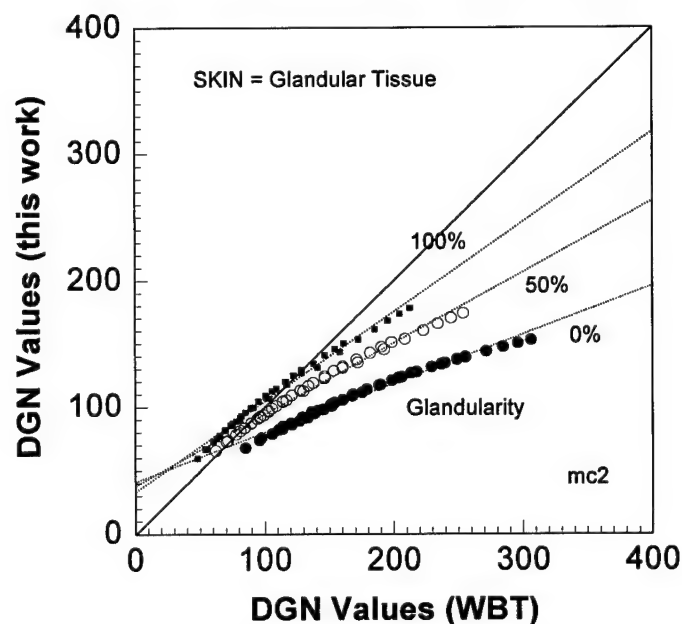
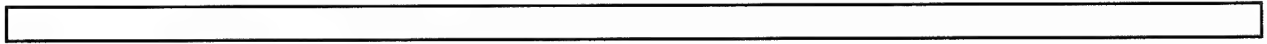


Figure 28.

Again, the DGN values of this work are compared against the work of Wu, Barnes, and Tucker (WBT). In this simulation, the skin was assumed to be equivalent to glandular tissue. It is evident from this and the previous figure that less-than-perfect correspondence between the DGN values was measured. These differences have been the focus of substantial effort on the part of the principal investigator, as discussed in the text.



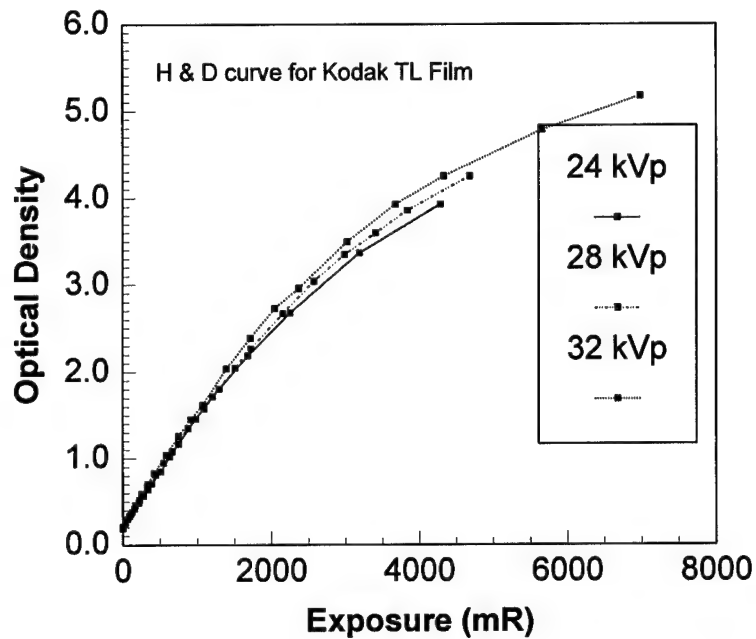


Figure 29.

The H&D curve for the Kodak TL film is illustrated for three different beam energies. Only a slight dependency on beam quality is observed in the H&D curves, and it is our intention to develop an energy dependent correction for measuring the exposure densitometrically.

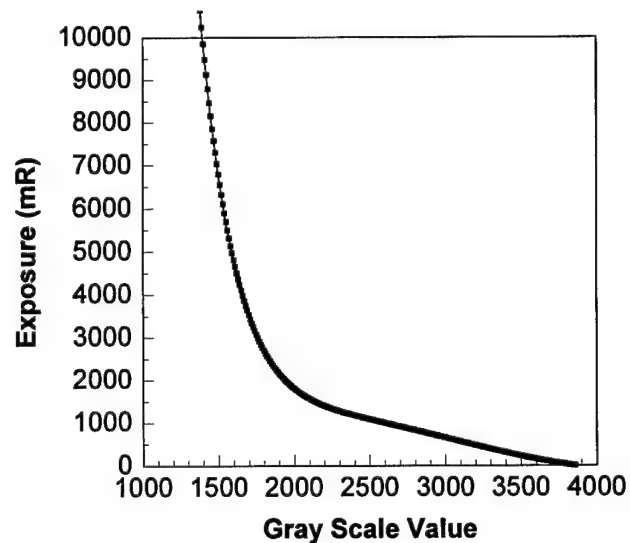


Figure 30.

The relationship between the incident exposure (mR) and the gray scale value produced by the Lumisys laser digitizer is illustrated in this figure. The curve shown here was fit using commercial software to an analytical function and used subsequently to convert digitized images to be linear with exposure.

Heel Effect

Rank 1 Eqn 18 $z=a+bx+cx^2+dy+ey^2+fy^3$
 $r^2=0.99072673$ DF Adj $r^2=0.99051834$ FitStdErr=0.79195433 Fstat=5726.4525

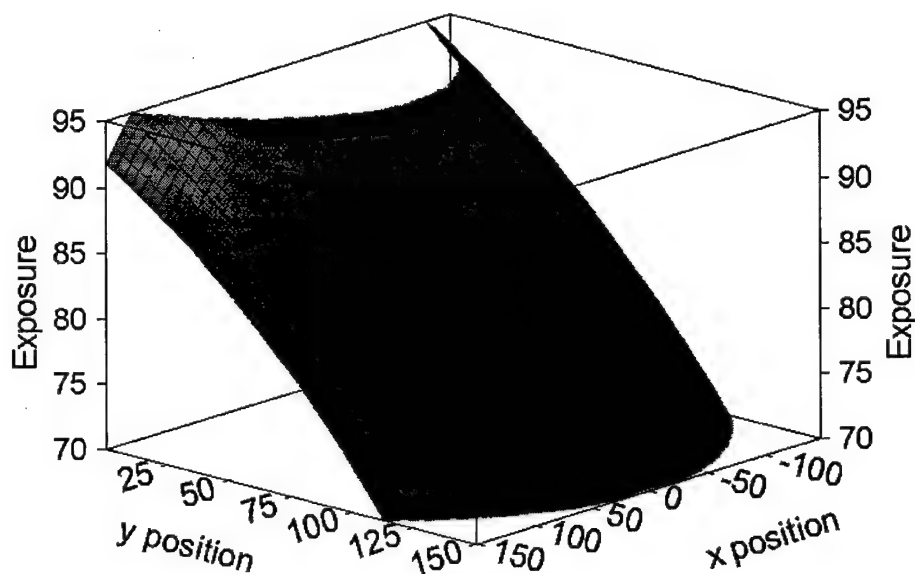


Figure 31.

A flat field image was acquired using TL film, and was converted to exposure using the curve shown in the previous figure. The exposure distribution was then fit using the polynomial equation illustrated in this figure. This figure illustrates the exposure distribution resulting from the heel effect on a GE 500T mammography system in our research laboratory. This is just one example of the type of data which we hope to incorporate into our Monte Carlo procedures, such that they produce realistic results which correlate well with measured data.

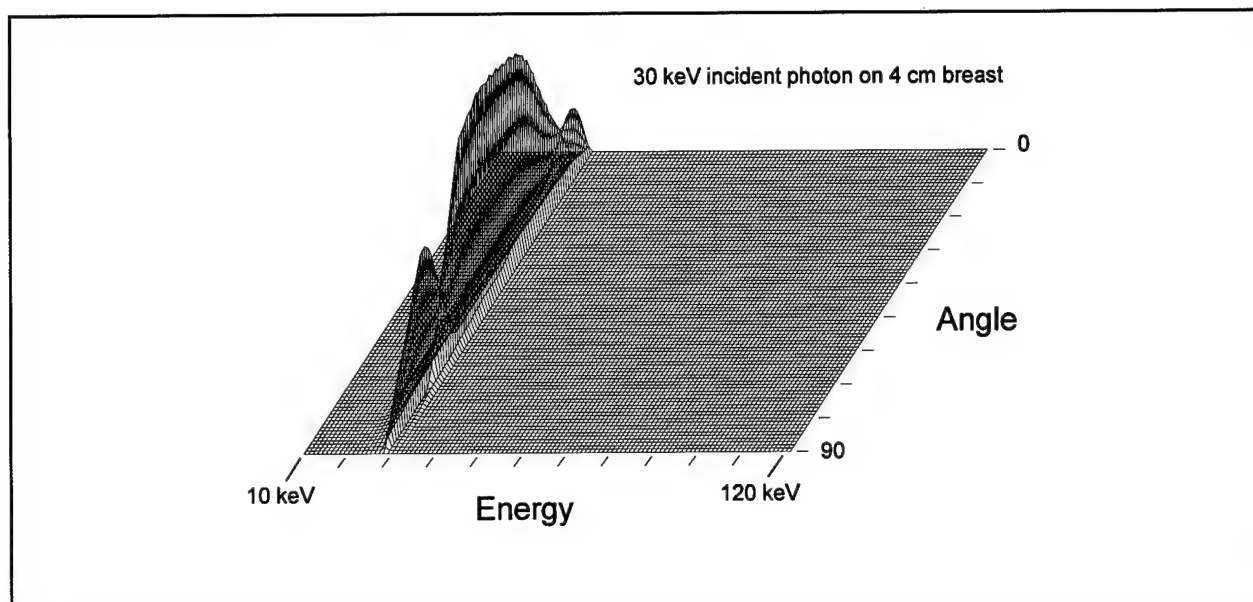


Figure 32.

A typical result from the Monte Carlo simulation routine developed in our laboratory. This figure illustrates the energy and angle distribution of x-ray photons emitted on the detector side of a 4 cm breast. A 30 keV incident x-ray beam consisting of 10,000,000 photons was incident upon the breast.

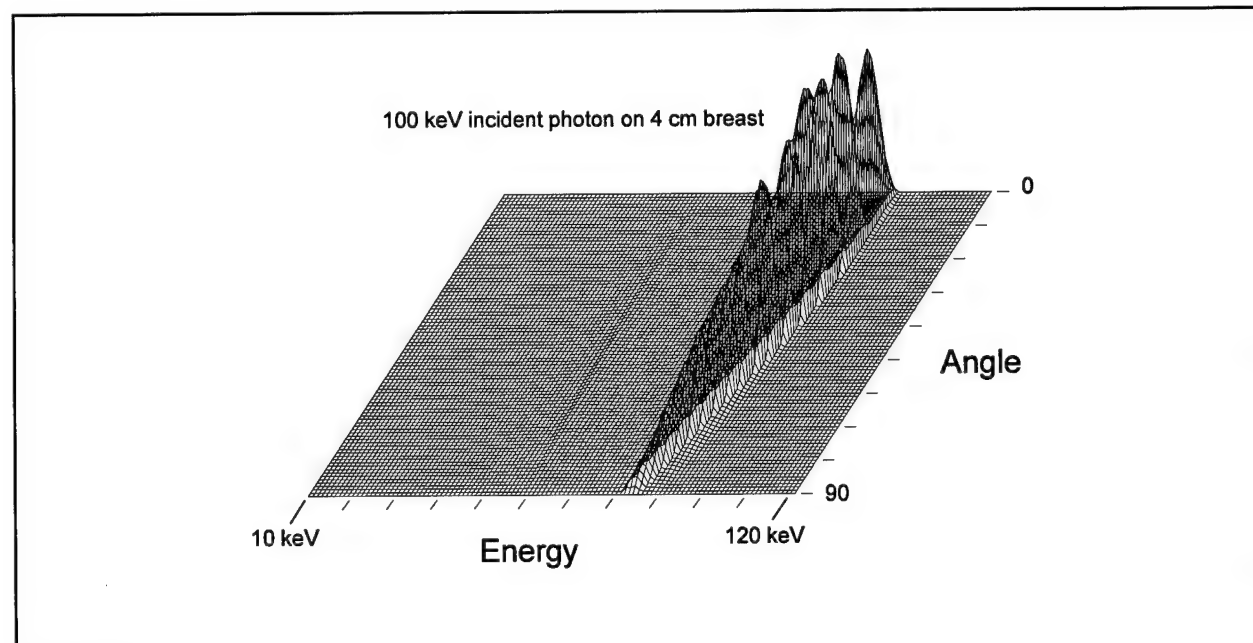


Figure 33.

An energy versus angle diagram of the x-ray photons emitted from the exit side of a 4 cm breast which has been exposed to a 100 keV incident x-ray photon beam. As expected, photons exiting at higher angles (those approaching 90°) have lost more energy in (Compton) scattering, and therefore the energy of the emitted photons is reduced at higher angles of emission. The scalloped appearance of the ridge shown in this isometric plot is an artifact of the binning process (a quantization artifact).

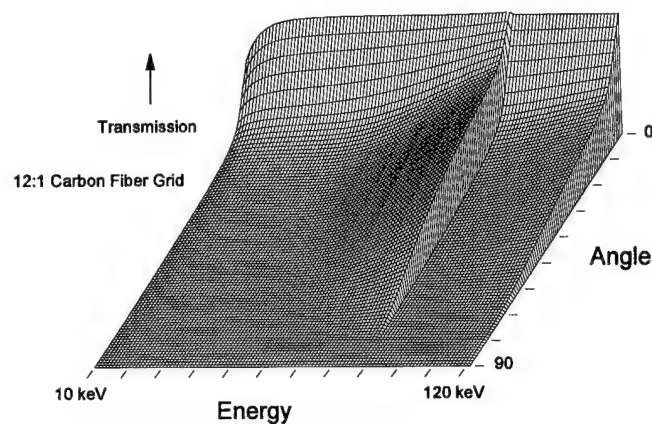


Figure 34.

This figure illustrates an isometric plot showing the transmission of a 12:1 carbon fiber inner spaced grid as a function of energy and angle of photons incident upon it. High transmission values are seen at low angles, as expected. The discontinuity visible at 88 keV is a result of the K edge of the lead strips in the grid.

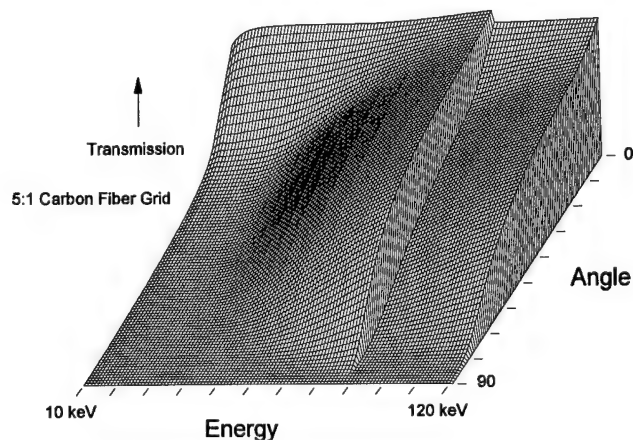


Figure 35.

An isometric plot showing transmission as a function of energy and angle for 5:1 carbon fiber grid, used typically in mammography. Substantially higher transmission occurs at higher angles (e.g. in the range from $\sim 10^\circ$ to 75°), suggesting that this grid is not adequate for use at the higher keV's used for dual energy mammography.



Figure 36.

A 50 kV radiographic image of some Lego blocks, BR12, calcium-chips, and tie-wraps, taken on the dual energy mammography system in our laboratory.

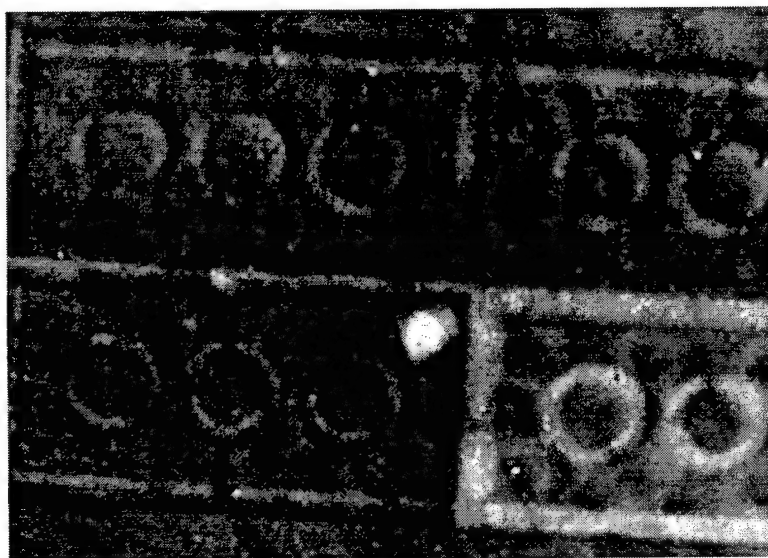


Figure 37.

A dual energy subtracted image of the Lego test phantom. Two large (~2 mm) calcifications are clearly visible. Some motion artifact is also apparent in the image, which explains the less than perfect subtraction of three of the Legos. These Legos are an assortment of new ones (purchased in the 1990's) and old ones (purchased in the 1960's). Since it is clear from the image that the lower right Lego brick is enhanced on this dual energy subtraction, we hypothesize that the lower right Lego is an older one, and is made with a different red pigment which has a higher effective atomic number than the newer pigment.

7. Conclusions

We are well on the way towards completing the Statement of Work in this grant. In the path towards evaluating the ultimate potential of dual energy mammography, we have chosen to take the long route, by focusing on details along the way. The development of an easy to use data base of attenuation coefficients, fully compared to those used historically in Monte Carlo work, the development of spectral models for general diagnostic and mammographic x-ray systems, and the analysis of fiber optical scintillating screens, are examples of these details.

We have demonstrated in this report that the software tools are in place to execute optimization procedures concerning the best x-ray spectra (tasks 1.1 and 1.2) and the best anti-scatter approach (task 1.4). Task 1.3 was essentially made irrelevant by our decision to move to a dual-kV pulse system, from the original binary screen dual energy approach. Once we are able to fully validate our Monte Carlo code with experimental results, the energy deposition and scattering tables will be solidified and the subsequent optimization code rerun on this proven data. We are also scheduled to discuss the Monte Carlo results of the Wu, Barnes and Tucker paper²³ with Dr. Gary Barnes shortly, after he has returned from a trip in South America (the PI arranged this informally with Dr. Barnes at the AAPM meeting in Milwaukee in August).

Task 2 (tasks 2.1 and 2.2) has been completed, and while we are continuing to update our camera configuration based on measurements of performance of the detector, the system is up and running and is ready for experimentally verifying the Monte Carlo results when they become available.

Task 3.1 (MTF measurements) and Task 3.2 (DQE measurements) have been performed and demonstrated in this report. We are using these results to further refine the configuration of the detector system (task 2), and thus a dynamic feedback exists between tasks 2 and tasks 3. Comparison to digitized film images (task 3.3) is relatively simple, and will be performed once the final optimal acquisition parameters are identified.

The bulk of the final phase of this research, task 4, is to commence in this coming (fourth) year of the project. Both tasks 4.1 and 4.2 are dependent upon the existence of dual energy image data sets, and so these software projects are dependent upon the hardware developments in the previous tasks.

We anticipate that the Monte Carlo experimental verification experiments will take us into December, and subsequent optimization dual energy procedures will then require perhaps a month. Then in January, we can concentrate on the completion of task 4 during the spring.

8. References

1. Boone JM, Tecotzky M, Alexander GM: Binary screen detector system for single-pulse dual-energy radiography. *Radiology* 1992;183:863-870.
2. Boone JM: X-ray spectral reconstruction from attenuation data using neural networks. *Med Phys* 1990;17:647-654.
3. Boone JM: The three parameter equivalent spectra as an index of beam quality. *Med Phys* 1988;15:304-310.
4. Boone JM: Equivalent spectra as a measure of beam quality. *Med Phys* 1986;13:861-868.
5. Tucker DM, Barnes GT, Wu XZ: Molybdenum target x-ray spectra: a semiempirical model. *Med Phys* 1991;18:402-407.
6. Tucker DM, Barnes GT, Chakraborty DP: Semiempirical model for generating tungsten target x-ray spectra. *Med Phys* 1991;18:211-218.
7. Fewell TR, Shuping RE, Healy KE: Handbook of computed tomomgraphy x-ray spectra. *HHS Publication (FDA)* 1978;81-8162:
8. Fewell TR, Shuping RE: Handbook of mammographic x-ray spectra. *HEW Publication (FDA)* 1978;79-8071:
9. Johns PC, Yaffe MJ: Theoretical optimization of dual-energy x-ray imaging with application to mammography. *Med Phys* 1985;12:289-296.
10. Boone JM, Shaber GS, Tecotzky M: Dual-energy mammography: a detector analysis. *Med Phys* 1990;17:665-675.
11. Deslattes RD, Levin JC, Walker MD, Henins A: Noninvasive high-voltage measurement in mammography by crystal diffraction spectrometry. *Med Phys* 1994;21:123-126.
12. Hudson LT, Deslattes RD, Henins A, Chantler CT, Kessler EG, Schweppe JE: A curved crystal spectrometer for energy calibration and spectral characterization of mammographic x-ray sources. *Med Phys* 1996;23:1659-1670.
13. Yu T, Boone JM: Lens coupling efficiency: derivation and application under differing geometrical assumptions. *Med Phys* 1997;24:565-570.
14. Yu T, Sabol JM, Seibert JA, Boone JM: Scintillating fiber optic screens: a comparison of MTF, light conversion efficiency, and emission angle with Gd₂O₂S:Tb screens. *Med Phys* 1997;24:279-285.

15. Boone JM, Seibert JA: An accurate method for computer-generating tungsten anode x-ray spectra from 30 to 140 kV. *Medical Physics* 1997;24:
16. Boone JM, Seibert JA: A comparison of mono- and poly-energetic x-ray beam performance for radiographic and fluoroscopic imaging. *Med Phys* 1994;21:1853-1863.
17. Boone JM: Parametrized x-ray absorption in diagnostic radiology from Monte Carlo calculations: implications for x-ray detector design. *Med Phys* 1992;19:1467-1473.
18. Boone JM: Color mammography. Image generation and receiver operating characteristic. *Invest Radiol* 1991;26:521-527.
19. Boone JM, Seibert JA: Monte Carlo simulation of the scattered radiation distribution in diagnostic radiology. *Med Phys* 1988;15:713-720.
20. Boone JM, Seibert JA: An analytical model of the scattered radiation distribution in diagnostic radiology. *Med Phys* 1988;15:721-725.
21. Boone JM, Chavez AE: Comparison of x-ray cross sections for diagnostic and therapeutic medical physics. *Med Phys* 1996;23:1997-2005.
22. Boone JM, Fewell TR, Jennings RJ: Molybdenum, rhodium, and tungsten anode spectral models using interpolating polynomials with application to mammography. *Medical Physics* 1997;25:
23. Wu X, Barnes GT, Tucker DM: Spectral dependence of glandular tissue dose in screen-film mammography. *Radiology* 1991;179:143-148.
24. Wu X, Gingold EL, Barnes GT, Tucker DM: Normalized average glandular dose in molybdenum target-rhodium filter and rhodium target-rhodium filter mammography. *Radiology* 1994;193:83-89.
25. Hammerstein GR, Miller DW, White DR, Masterson ME, Woodard HQ, Laughlin JS: Absorbed radiation dose in mammography. *Radiology* 1979;130:485-491.
26. Seibert JA, Boone JM: X-ray scatter removal by deconvolution. *Med Phys* 1988;15:567-575.
27. Boone JM: Scatter correction algorithm for digitally acquired radiographs: theory and results. *Med Phys* 1986;13:319-328.
28. Mickish DJ, Beutel J: The determination of x-ray phosphor scintillation spectra. *SPIE* 1990;1231:327-336.

Appendix A

This is a compilation of the publications produced by funding from this project to date. Several other publications are in preparation and will be submitted before the end of the year.

1. JM Boone, T Yu, J.A. Seibert, Sinusoidal modulation analysis for optical system MTF measurements, Med. Phys 23, 1955-1963 (1996)
2. JM Boone and AE Chavez, Comparison of x-ray cross sections for diagnostic and therapeutic medical physics, Med. Phys 23, 1997-2005 (1996)
3. T Yu, JM Sabol, JA Seibert, and JM Boone, Scintillating fiber optic screens: A comparison of MTF, light conversion efficiency, and emission angle with $Gd_2O_2S:Tb$ screens, Med. Phys. 24, 279-285 (1997)
4. T Yu and JM Boone, Lens coupling efficiency: derivation and application under differing geometrical assumptions, Med. Phys. 24;565-570, 1997
5. JM Sabol and JM Boone, Monte Carlo simulation of photon transport within a hybrid grid detector system for digital mammography, Proc SPIE 3032: 266-274 (1997)
6. T Yu, JM Sabol, JA Seibert, and JM Boone, Imaging consideration for scintillating fiber optic screens, Proc SPIE 3032:137-141 (1997)
7. JM Boone and JA Seibert, A tungsten anode spectral model using interpolating polynomials and tabulation of x-ray quantum fluence, Medical Physics, (in press)
8. JM Boone, TR Fewell and RJ Jennings, Molybdenum, Rhodium, and Tungsten anode spectral models using interpolating polynomials with application to mammography, Medical Physics (in press)

Appendix B

Derivation of the energy calibration equation

As given by Deslattes^{11,12}, we have the following equations:

$$E = \frac{n\Lambda R}{2dS \sin \alpha} \quad (1)$$

$$D = S \cdot \frac{\sin \alpha}{\cos \gamma} \quad (2)$$

where n is the order of refraction in the crystal, Λ is the energy-wavelength conversion constant and has the value 1.23984244 nm·keV, and d is the lattice spacing of the crystal. The other terms are defined in Figure A-1. The $\cos \gamma$ is given in terms of α by:

$$\cos \gamma = \left[1 - 2 \frac{S^2}{R^2} \sin^2 \alpha \right] \cos \alpha + 2 \frac{S}{R} \sin^2 \alpha \sqrt{1 - \frac{S^2}{R^2} \sin^2 \alpha} \quad (3)$$

The equation that we want is one which presents a direct relationship between E and D . From equations (1) and (2):

$$E = \frac{n\Lambda R}{2d \cos \gamma D} \quad (4)$$

Let $\cos \gamma = x$, we have:

$$\sin \alpha = \frac{D}{S} x$$

$$\cos \alpha = \left[1 - \frac{D^2}{S^2} \cdot x^2 \right]^{\frac{1}{2}}$$

From equation (3):

$$x = \left[1 - 2 \frac{D^2}{R^2} x^2 \right] \left[1 - \frac{D^2}{S^2} x^2 \right]^{\frac{1}{2}} + 2 \frac{D^2}{RS} x^2 \left[1 - \frac{D^2}{R^2} x^2 \right]^{\frac{1}{2}} \quad (5)$$

$$\therefore \quad \frac{D^2}{S^2} x^2 \ll 1, \quad \frac{D^2}{R^2} x^2 \ll 1$$

$$\therefore \quad \left[1 - \frac{D^2}{S^2} x^2 \right]^{\frac{1}{2}} = 1 - \frac{1}{2} \cdot \frac{D^2}{S^2} x^2$$

$$\left[1 - \frac{D^2}{R^2} x^2 \right]^{\frac{1}{2}} = 1 - \frac{1}{2} \cdot \frac{D^2}{R^2} x^2$$

So the equation (5) becomes:

$$x = 1 - \frac{D^2}{2S^2} x^2 - \frac{2D^2}{R^2} x^2 + \frac{D^4}{R^2 S^2} x^4 + \frac{2D^2}{RS} x^2 - \frac{D^4}{R^3 S} x^4 \quad (6)$$

$$\therefore \quad \frac{D^4}{R^2 S^2} x^4 \approx \frac{D^4}{R^3 S} x^4 \approx 0$$

Equation (6) becomes:

$$\frac{D^2 (2S - R)^2}{2R^2 S^2} x^2 + x - 1 = 0 \quad (7)$$

By solving equation (7), we get:

$$x = \frac{RS \sqrt{R^2 S^2 + 2(2S - R)^2 D^2} - R^2 S^2}{(2S - R)^2 D^2} \quad (8)$$

Substituting equation (8) into equation (4), we get:

$$E = \frac{n\Lambda (2S - R)^2 D}{2dS \sqrt{R^2 S^2 + 2(2S - R)^2 D^2} - 2dRS^2} \quad (9)$$

X-ray photon amplitude calibration

The signal actually measured in the spectrometer is comprised of electrons, and this signal is linearly proportional to the light photons emitted by the scintillating screen. The light photon fluence emitted from the scintillating screen can be expressed as:

$$\Phi_q = \Phi_x \cdot F_1 \cdot F_2 \cdot F_3 \cdot F_4 \cdot F_5 \quad (1)$$

Where, the F_1 is x-ray transmittance of the silicon crystal, the F_2 is x-ray transmittance of the plastic cover on the top of the CCD, F_3 is x-ray absorption of the scintillating screen, F_4 is the conversion factor of the scintillating screen expressed as how many light photons per x-ray photon at each energy, and F_5 is the correction factor for the nonlinear relationship between x-ray energy and CCD pixel number shown in Figure A-2. These factors can be expressed as:

$$F_1 = \exp\left[-\left(\frac{\mu}{\rho}\right)_{\text{silicon}}(\rho t_{\text{eff}})_{\text{silicon}}\right]$$

$$F_2 = \exp\left[-\left(\frac{\mu}{\rho}\right)_{\text{plastic}}(\rho t_{\text{eff}})_{\text{plastic}}\right]$$

$$F_3 = 1 - \exp\left[-\left(\frac{\mu}{\rho}\right)_{\text{screen}}(\rho t_{\text{eff}})_{\text{screen}}\right]$$

F_4 is obtained by taking the differentiation of the x-ray energy over the CCD pixel number shown in Figure 1. F_5 is obtained by curve fitting the data published by D. Mickish and J. Beutel²⁸ shown in Figure 3. The x-ray photon fluence can be calculated by:

$$\Phi_x = \Phi_q \cdot \frac{1}{F_1} \cdot \frac{1}{F_2} \cdot \frac{1}{F_3} \cdot \frac{1}{F_4} \cdot \frac{1}{F_5}$$

All the correction factors are plotted in Figure A-2.

Since we were unable to measure the CCD response to the light photons before it was sealed, it is necessary to compare our calculated correction factor with measured ones to get these values. So that final x-ray photon fluence can be calculated as:

$$\Phi'_x = a \cdot \Phi_x + b$$

where value a is related to CCD camera gain factor, and value b is related to the CCD camera offset.

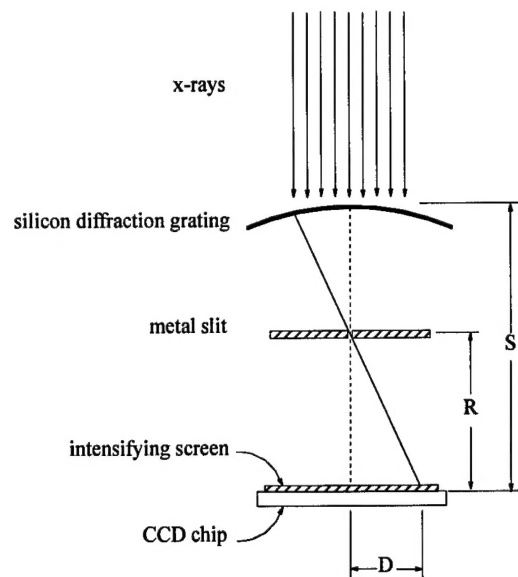


Figure A-1
A schematic diagram showing the various components of the Deslattes diffractometer is shown.

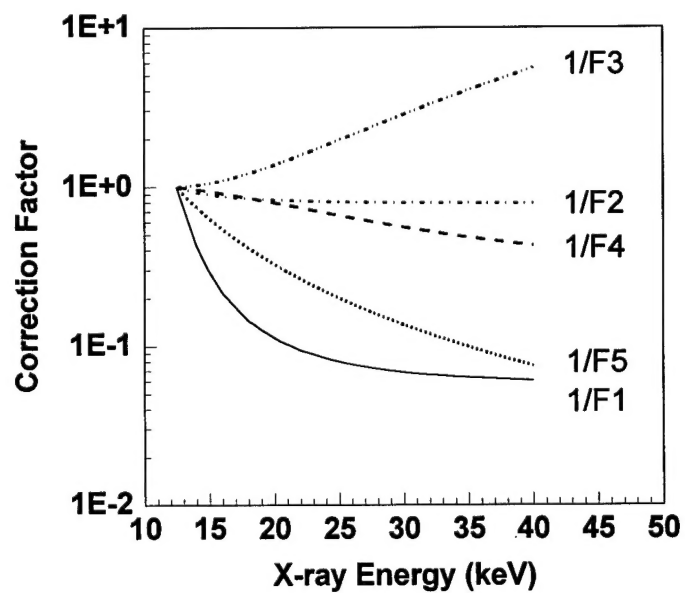


Figure A-2
The energy dependent correction factors (F1-F5) are illustrated in this figure.